The Cryosphere

Distribution of landfast, drift and glacier ice in Hornsund, Svalbard

Zuzanna M. Swirad[1], **A. Malin Johansson**[2], **and Eirik Malnes**[3]

[1]Institute of Geophysics, Polish Academy of Sciences, Warsaw, Poland
[2]Department of Physics and Technology, UiT The Arctic University of Norway, Tromsø, Norway
[3]NORCE Research AS, Oslo, Norway

Correspondence: Zuzanna M. Swirad (zswirad@igf.edu.pl) and A. Malin Johansson (malin.johansson@uit.no)

Abstract. Co-occurring landfast, drift and glacier ice in fjords respond to climate differently and have diverse impacts on the environment. Here we describe a new method to separate ice types in fjord environments on 2639 binary satellite-derived ice/open water maps at 50 m resolution. We used a set of thresholds to create near-daily maps of landfast, drift and glacier ice of Hornsund, Svalbard over 11.5 years (2 January 2012 to 29 June 2023). The ice was first divided into stationary and moving classes based on persistence in space (pixels) through time. The ice was then polygonised and the polygons were ascribed a set of parameters describing their class, time, size and location. Temporal and spatial constraints were imposed on landfast ice. Drift and glacier ice were split based on timing, location and size. Finally, the data were re-rasterised and refined at the pixel level. Over the 11.5 years, the fjord ice was classified as 53 % drift, 35 % landfast, 8.5 % glacier, 1.4 % uncertain ice type while 2.1 % was masked due to radar shadows. There was a great interannual variability in the length of sea ice and landfast ice seasons, and in ice type extent, with no clear long-term trend. Statistically significant negative correlation existed between the water temperature in the winter months (January–March) and the length of the sea ice and landfast ice season, as well as between the air temperature in winter months and sea ice and landfast ice coverage. Glacier ice coverage depended on air temperature in summer months (July–September) and water temperature autumn months (October–December) where lower temperatures enhanced ice persistence. The method can be adapted to other areas and used in a wide range of analyses including fjord hydrography, nearshore wave transformation or ecological studies.

1 Introduction

Landfast ice, drift ice and glacier ice in fjords can be collectively referred to as fjord ice. The fjord ice has a great impact on e.g. energy, heat and light exchange between the atmosphere and the water, habitat conditions, type and efficiency of coastal processes, boat operation, and snowmobile transport (Nomura et al., 2018; Ricker et al., 2021; Loose et al., 2024). Sea ice is classified by the Global Climate Observing System (GCOS) as an Essential Climate Variable. Presence, extent and timing of the different components of the fjord ice depend on different aspects of the climate. For instance, colder air and water temperatures result in a larger extent of landfast ice (Muckenhuber et al., 2016). Abundance of drift ice is related to water temperature (de Steur et al., 2023) but its spatial extent may also link to ocean currents, wind direction and wind speed (Spreen et al., 2020; Mezzina et al., 2024; Muilwijk et al., 2024). Finally, higher water temperatures contribute to more intense tidewater glacier calving and increased amounts of glacier ice (ice melangé, brash ice, growlers, bergy bits, icebergs) in fjords (e.g. Luckman et al., 2015; van Pelt et al., 2019). The different types of ice impact the environment differently as they are characterised by different salinity (sea vs freshwater), nutrient and sediment content (glacier ice brings material from terrestrial environment) and block shapes (sea ice for mammal resting spots, icebergs may be anchored to the seabed at larger depths, etc).

There is a pertinent lack of a collective analysis of fjord ice which may partly result from canonical separation of sea ice and glacier ice mapping efforts, and differences in scales and detection methods. However, because of their cumulative contribution to the fjord environment as well as interactions and feedback, it is important to approach fjord ice in a

comprehensive way. Some examples of the interactions between glacier ice and sea ice include in situ sea ice formation around glacier ice where surface water is cooled (Styszyńska and Rozwadowska, 2008) or a decrease in glacier calving in times of high sea ice concentration (Pętlicki et al., 2015).

The automated mapping of ice extent in fjord environments using synthetic aperture radar (SAR) satellite imagery has been limited, compared to the mapping efforts in the open ocean. The likely causes include the topography impact on radar shadowing, ocean surface wind patterns caused by tunnelling effects from the varying fjord side topography, mixed land/water pixels, tidal effect and presence of rocks and islands. Moreover, the different fjord ice types are characterised by similar radar backscatter values and, even if mapped collectively, the abundance of ice is difficult to relate to climate forcings (Swirad et al., 2024a).

The main goal of this study was to develop an automated method to map landfast, drift and glacier ice in fjord environments. To do so, we extended near-daily binary ice/open water maps for Hornsund, Svalbard (Swirad et al., 2023a) back in time to include three more sea ice seasons (Swirad et al., 2024b). We then used a set of calibrated thresholds to split the fjord ice into ice types. The maps cover the southern part of Svalbard around the Polish Polar Station (PPS) Hornsund and span over 11.5 seasonal cycles, January 2012–June 2023. The length of the dataset combined with extensive in situ measurements of air and water temperature enabled us to analyse seasonal and inter-annual trends and relate them to local climatological changes.

2   Study area

Hornsund is a $\sim 300\,\mathrm{km^2}$ fjord in south-western Spitsbergen, Svalbard. It has a $\sim 12\,\mathrm{km}$ wide opening to the Greenland Sea. The fjord can be split into the main basin ($\sim 152\,\mathrm{km^2}$) and the inner bays: Burgerbukta ($\sim 34\,\mathrm{km^2}$), Brepollen ($\sim 96\,\mathrm{km^2}$) and Samarinvagen ($\sim 18\,\mathrm{km^2}$). The average and maximum depths are ~ 100 and $\sim 240\,\mathrm{m}$, respectively (Fig. 1), with a tidal range of 0.75 m. The Sørkapp Current brings cold and fresh Arctic waters from the Barents Sea while the West Spitsbergen Current transports warm and saline Atlantic Water (Saloranta and Svendsen, 2001; Promińska et al., 2018).

The sea ice in Hornsund has a dual origin – it is either brought in from the Barent Sea with the Sørkapp Current or formed in situ by seawater freezing. Pack ice was present annually at the entrance to the fjord from October/December till May/July until 2005, when a regime shift occurred making it episodic in the Hornsund area (Herman et al., 2025). A decrease in landfast ice coverage after 2005 was also observed (Muckenhuber et al., 2016). Between 2014 and 2023 (nine sea ice seasons) the landfast ice started forming between December and March (average on 4 February) and disappeared between May and July (average on 17 June) (Swirad et al.,

2024a). Spatially, higher and more consistent ice coverage characterised inner bays compared to the main basin. The highest coverage was in March in the main basin and in April in the bays, and there was a large interannual variability (Swirad et al., 2024a).

The mean daily air temperature at the PPS Hornsund weather station averaged $-3.7\,^\circ\mathrm{C}$ in 1979–2018, but there has been an increase in mean annual air temperature by $1.14\,^\circ\mathrm{C}$ per decade with the largest increase in winter months. The easterly (from the inner fjord) winds dominated (mean direction 124°) and the mean wind speed was $5.5\,\mathrm{m\,s^{-1}}$ (max $7.1\,\mathrm{m\,s^{-1}}$ in February). Precipitation increased by $6.2\,\mathrm{mm\,yr^{-1}}$ (Wawrzyniak and Osuch, 2020). Swell from south-southwest (open Greenland Sea) and locally generated short wind waves dominate with mean summer and winter offshore significant wave height of 1.2–1.3 and 2.6–2.7 m, respectively, which decrease to 0.2–0.4 and 0.3–0.5 m at the nearshore of the main basin (Wojtysiak et al., 2018; Herman et al., 2019; Swirad et al., 2023b). Pack ice with the concentration $> 50\,\%$ at the entrance to Hornsund effectively attenuates swell entering the fjord which results in lower significant wave height and longer wave period (Herman et al., 2025).

There are 16 tidewater glaciers in Hornsund which had the cumulative ice cliff length of 34.7 km in 2010. The glaciers retreated by $70 \pm 15\,\mathrm{m\,yr^{-1}}$ in 2001–2010 (Błaszczyk et al., 2013). Swirad et al. (2024a) observed a secondary peak in fjord ice coverage in October, ascribing it to the glacier calving.

3   Methods

3.1   Binary ice/open water classification

The ice/open water maps are based on RADARSAT-2 (RS-2) and Sentinel-1A/B (S-1) SAR scenes from Hornsund between January 2012 and June 2023. The S-1 dataset, processing workflow and validation against optical imagery were described in Swirad et al. (2024a) and here we only outline the RS-2 image processing.

3.1.1   RADARSAT-2 data processing

In total 797 RS-2 scenes fully covered the Hornsund fjord between 2 January 2012 and 1 March 2016, of which 638 (80 %) were used for the ice mapping. Rejected scenes had either poor quality, lacked one of the polarization channels or occurred on the same day as a better quality scene. The remaining scenes had an average temporal frequency of 2.38 d for the entire period and 1.74 d until 18 November 2014 after which the acquisition became sporadic due to the S-1 data coverage over the area. The scenes were geocoded on a fixed grid with extent of X: 499–544 km and Y: 8531–8559 km (WGS84, UTM33N) and $50 \times 50\,\mathrm{m}$ pixel spacing using GSAR software (Larsen et al., 2006). For each scene
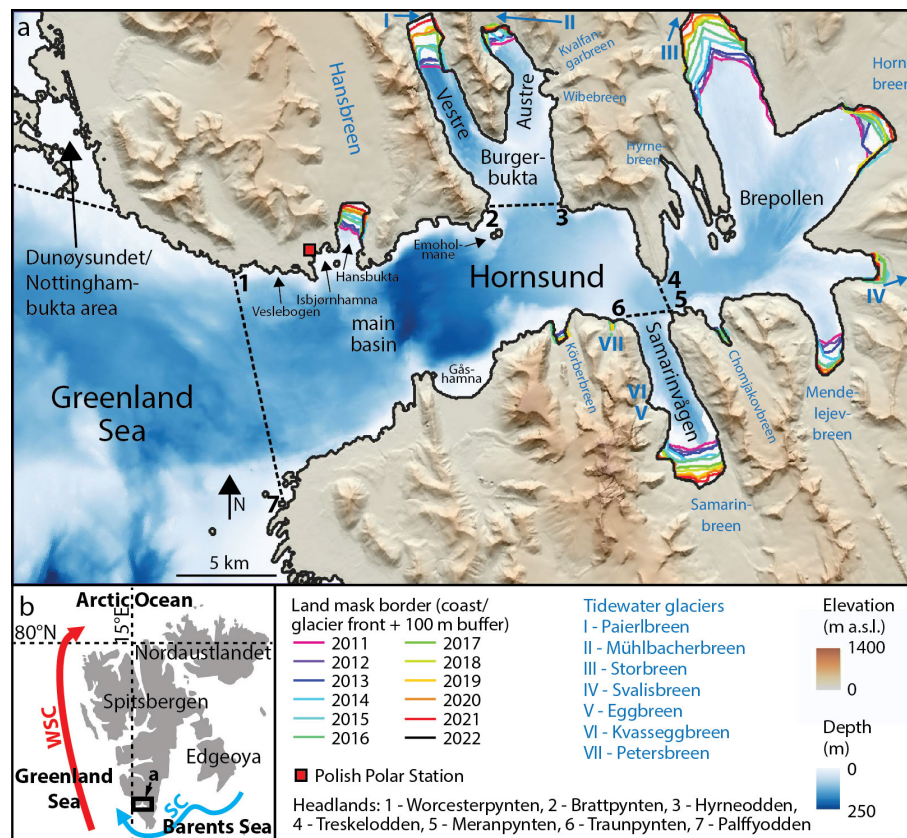
Figure 1. Study area: **(a)** Hornsund, **(b)** Svalbard. WSC – West Spitsbergen Current. SC – Sørkapp Current. DEM courtesy of the Polar Geospatial Center; bathymetry IBCAO V5.0 Grid at 100 m and Norwegian Hydrographic Service at 5 m.

HH- and HV-channel radar backscatter sigma nought and incidence angle GeoTIFF rasters were created.

The Norwegian Polar Institute's land shapefile (NPI, 2014) was used to create a land mask that was updated annually using SAR image from 1 July (or the first available thereafter) to account for fjord area increase resulting from tidewater glacier retreat. Envisat ASAR scene was used for the 2011 mask, RS-2 for the 2012–2014 masks and S-1 for the subsequent masks. Each mask was applied on the 1 July–30 June period. Additionally, a 100 m buffer was added along the coast to exclude the tidal zone, with a larger buffer area in the shallow, deltaic Dunøysundet/Nottinghambukta (DN) area (for location see Fig. 1).

Automated segmentation and classification followed the method developed by Cristea et al. (2020), and adapted to the Svalbard fjord environment by Johansson et al. (2020) and to Hornsund by Swirad et al. (2024a). A segmentation algorithm uses three raster layers: two polarization channels and an incidence angle layer. The algorithm considers the surface-specific intensity decay rate with increased incidence angle and it splits the image area into discontinuous segments using the traditional expectation-maximisation algorithm until the Pearson-style goodness-of-fit test is passed. Markov-random-field-based contextual smoothing and filter-ing were applied. The images were multi-looked 3×3 and log-transformed (Johansson et al., 2020). The number of segments ranged 3–6 with the majority (62 %) of 5 segments. In 631 cases (99 %) both HH and HV channels were used, five times only the HH channel and twice only the HV channel.

The 3–6 discontinuous segments were manually classified as "ice" (1) or "open water" (0). Of the 638 scenes, 499 (78 %) did not require any modifications. For the remaining scenes the segments were polygonised in QGIS (v3.28) and some polygons were added or removed from the ice class (minor manual editing of 77 scenes, 12 %) or entirely manually picked (62 scenes, 9.7 %). The resulting binary maps are available in the PANGAEA repository (Swirad et al., 2024b) and accompanied by a document outlining the scenes and channels used, the number of segments and the level of manual editing.

3.1.2 RADARSAT-2 and Sentinel-1 data collation

On the top of the above described 638 binary maps based on RS-2 imagery, we used 2031 binary maps based on S-1 archive between 14 October 2014 and 29 June 2023 available in the PANGAEA repository (Swirad et al., 2023a).

Consistency in sea ice detection between different sensors was verified by Johansson et al. (2020) in Kongsfjorden and Rijpfjorden. Here, we used 29 pairs of binary maps available for the same day. The correlation coefficient for the ice extent from the RS-2 and S-1 image pairs is 0.96 and the RMSE is $52.6\,\mathrm{km}^2$ (Fig. 2). The differences may be partly attributed to the ice drift and the time difference in image acquisition with RS-2 scenes taken either around 05:30–06:30 or 15:30–16:00 UTC and S-1 scenes taken around 06:00–06:30 UTC. 72 % ice pixels overlap even though the ice drift makes pixel-by-pixel comparison difficult and underscores the performance. Slight differences in the detected sea ice may stem from a lower Noise Equivalent Sigma Zero (NESZ) for RS-2 (-26.5 to -31 dB) compared to S-1 (-22 dB) (https://sentiwiki.copernicus.eu/web/s1-mission, last access: 31 July 2025), making it comparably somewhat easier to identify newly formed sea ice in the RS-2 images and somewhat less sensitive to wet snow. Sight differences in the incidence angle between the images may also result in smaller sensor dependent differences in the binary maps.

The two datasets were combined into a single time series of 2639 ice maps. For the days when both RS-2 and S-1 maps were available, RS-2 scenes were used because of the lower noise floor (https://earth.esa.int/eogateway/documents/20142/0/Radarsat-2-Product-description.pdf, last access: 30 July 2025) and visual inspection of the scenes. The 2018-12-25 (S-1) map was omitted because of a size mismatch.

3.2 Separation of ice types

Although they are similar in backscatter values, we expected the types of ice (landfast, drift, glacier) to be separable by their persistence through time, location in the bay-sea domain, timing in the year, size and shape. For example, landfast ice is generally present in the bays over an extended time period, mostly in spring. Conversely, drift ice is mostly present in the open Greenland Sea and in the main basin of Hornsund, where its location changes at a daily to weekly scale and it is present mostly in winter and spring though it may occur at different periods too. Finally, glacier ice is predominantly present in summer and autumn (Luckman et al., 2015), mostly in the bays though it sometimes drifts out to the main basin. Here we describe a workflow of separating types of fjord ice based on thresholds set based on the familiarity with the study area and understanding of the physical processes (Fig. 3).

3.2.1 Fjord ice split into stationary and moving ice classes

The persistence of ice in single locations (pixels) over consecutive days was first determined under the assumption that landfast ice persists in the same locations longer than drift and glacier ice. The aim was to divide ice into "stationary" and "moving" based on uninterrupted occurrence in the same

locations over a certain number of consecutive days. If the ice was present in a pixel on every day over these periods, it was classified as "stationary" ice. Otherwise, it was classified as "moving" ice. To optimize the number of days for the separation, a 13-month subset of maps (July 2018–July 2019; $n = 293$) was analysed. The total area of stationary and moving ice was extracted for bays and open Greenland Sea (as delimited in Fig. 1) based on an uninterrupted persistence during 5, 10, 15 and 20 subsequent days. Figure 4 shows that in the bays the area of moving ice was dynamic throughout the year likely reflecting the glacier and drift ice fluxes as well as landfast ice edge fluctuations. Conversely the stationary ice was consistently absent during the summer and autumn months and present during the late winter and spring months, with the exception of the 5 d persistence when ice appeared stationary in early autumn. In the open sea, the ice was present nearly exclusively in winter/spring. A 5 and 10 d persistence thresholds over this area meant that stationary ice was present despite the lack of locations for the landfast ice to form. We believe that these are the locations of recurrent presence of drift ice or where drift ice was temporarily halted. The 20 d threshold resulted in the highest amount of moving ice extent (Fig. 4), though the difference to the 15 d threshold was limited. The 15 d threshold implies one to four repeat cycles for S-1, meaning that a range of incidence angles may be covered in each period. Based on these observations we set 15 d as a threshold for separating moving and stationary ice.

3.2.2 Radar shadow masks

Each orbit is characterised by a different area of uncertainty resulting from radar shadow and layover by topography. With the larger incidence angle the mountain shadows cover larger fjord areas. To mask out areas that may be erroneously classified as ice, radar masks were extracted for each used orbit separately ($n = 30$ for RS-2 and $n = 11$ for S-1). A 200 m buffer was applied around the shadowed zones (Fig. 5a–b). The radar masks were applied on the stationary/moving ice rasters, so that if ice pixels were within the masked area, they were given a separate class "masked" and were not edited thereafter (Fig. 5c).

3.2.3 Polygon classification

The annually-updated (July–June) maps of aerial distance from land, bays and glacier fronts, and the single maps of aerial distance from the open sea and to Dunøysundet/Nottinghambukta (DN) area were created in QGIS (Fig. 6). The masked moving and stationary ice maps were polygonised in such a way that all touching pixels of the same class (moving/stationary) were put into the same polygon. The polygons were characterised by a number of parameters: ice class (moving/stationary), date, surface area, mean, minimal and maximal distance from the sea, bays, land, glacier fronts and
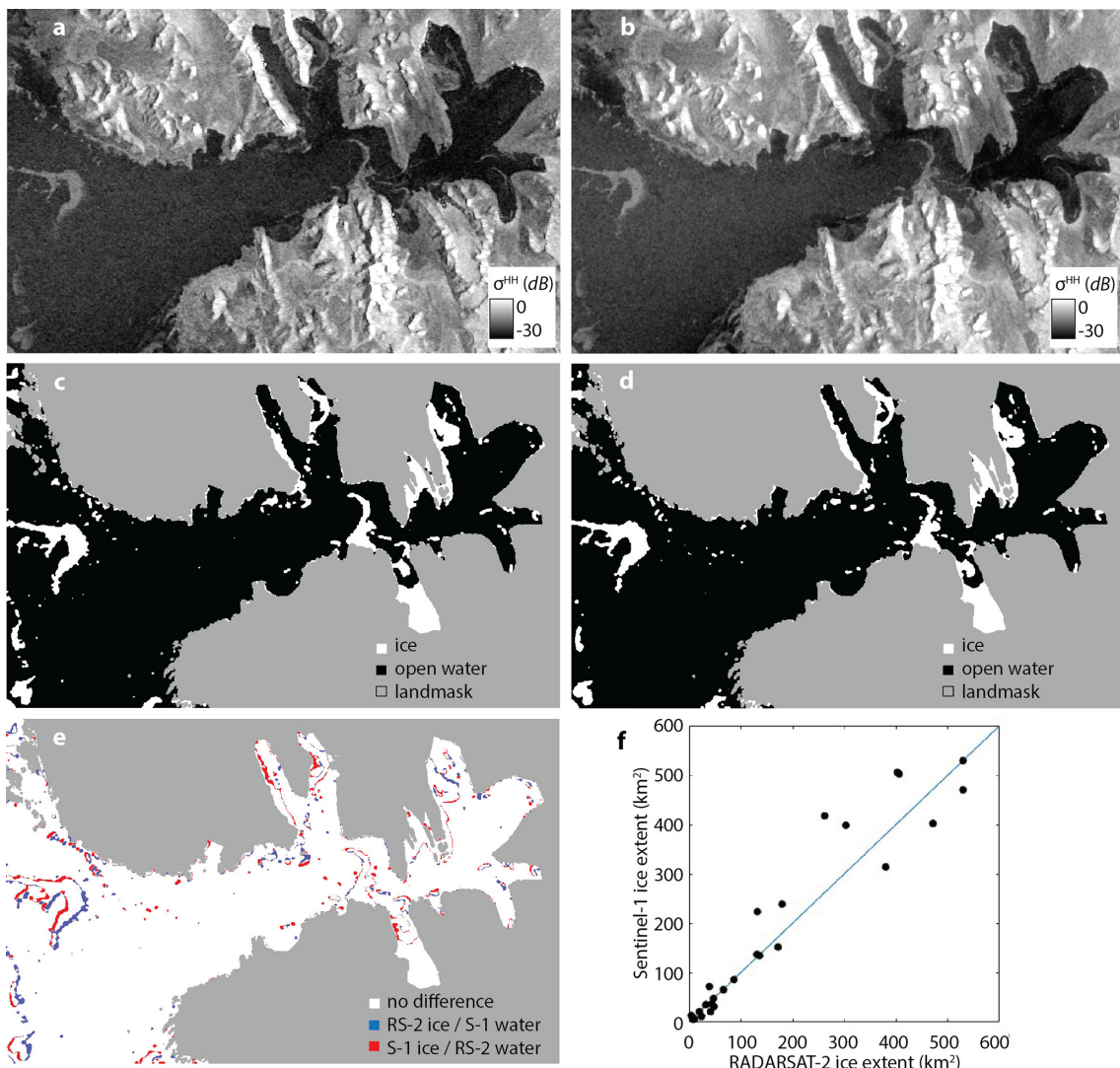
Figure 2. Inter-sensor comparison of fjord ice mapping: **(a)** RADARSAT-2 (RS-2) scene RS2_SCWA_20150105_053323_DES_152, **(b)** Sentinel-1 (S-1) scene S1_EWM_20150105_054924_DES_110, **(c)** RS-2 binary map, **(d)** S-1 binary map, **(e)** difference map, **(f)** fjord ice extent for the 29 overlapping dates.

the DN area, and the minimal class value within a 50 m buffer (Table 1).

The importance of the inclusion of distance measures can be observed in Fig. 7. The highest proportion of ice was present in the bays (A in Fig. 7a). The second peak of stationary ice in the open sea was likely caused by the continuous flow (re-occurrence of drift ice) or locally halted drift ice or, to a lesser extent, landfast ice presence in the vicinity to the DN area (B in Fig. 7a). The intermediate peak for both ice classes (C in Fig. 7a) may indicate sheltered Hansbukta/Isbjørnhamna area and Gåshamna where landfast ice might have formed and drift ice could have persisted. In the former area the peak might also reflect glacier ice. The dominance of moving ice closer to the sea reflects the pack ice drifting from the Greenland Sea, while a higher proportion

of stationary ice present at 15–20 km from the sea indicates the bays (D in Fig. 7b). Both ice classes occurred most often close to the bays and to the land, which is not surprising given the sheltered character of these locations where the landfast ice could form and persist, drift ice could have been pushed from the main basin or formed from breaking up of the landfast ice, and glacier ice could have been produced (E in Fig. 7c). At glacier fronts located in the deepest parts of the bays favourable conditions existed for both the landfast ice to form and the glacier ice to persist. There is, however, quite a high variability in density distribution for various distances from the glacier fronts. This may be because Hornsund bays are relatively large, and a sheltered area stretches far from the glacier fronts. For instance, the entrance to Brepollen, a place of abundant landfast and drift ice, is located 8–10 km
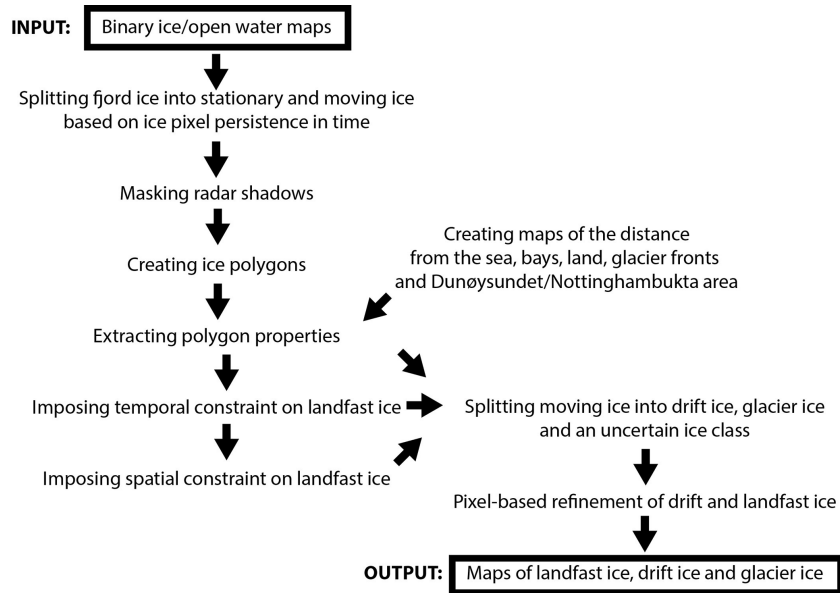
Figure 3. Fjord ice type separation workflow.
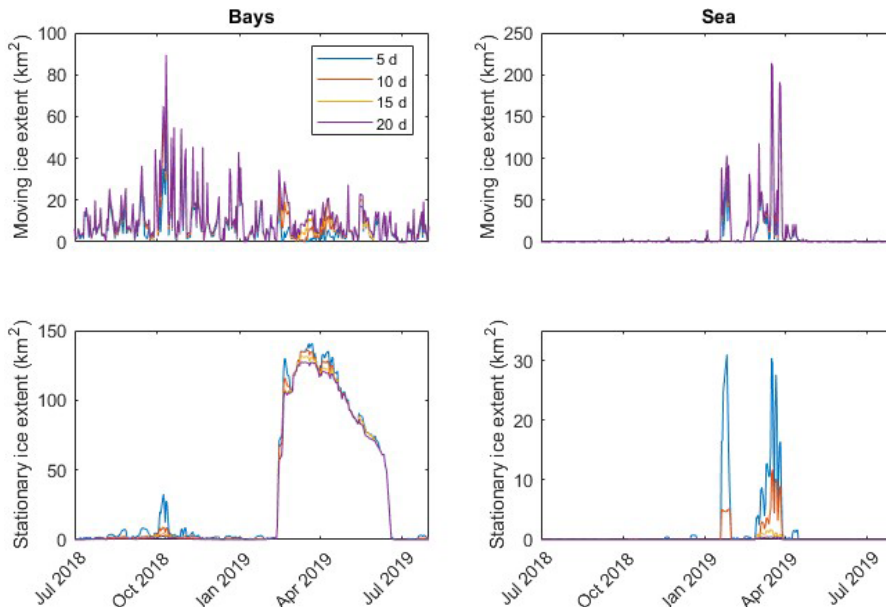
Figure 4. The extent of moving and stationary ice between 1 July 2018 and 31 July 2019 depending on the minimal number of consecutive days of ice presence in the bays and open sea as delimited in Fig. 1.

from the glacier fronts (F in Fig. 7d). The peak at $\sim 16\,\mathrm{km}$ from the glacier fronts indicates the DN zone (G in Fig. 7d). Finally, the DN area is also ice-rich with further peaks representing individual bays that are generally zones of both stationary and moving ice concentration (H in Fig. 7e).

The timeseries of the extent of the stationary and moving ice shows that the 15 d persistence threshold provided a rough separation between landfast (stationary) and drift/glacier (moving) ice (Fig. 8a). The consistent extent of

stationary ice from late winter to the end of spring agrees with the timing of the landfast ice (Swirad et al., 2024a). The limited extent and duration of the landfast ice in winters with high air temperatures (2011/2012 and 2013/2014) are well captured (A in Fig. 8a). The moving ice in summer and autumn represents glacier ice (B in Fig. 8a). Drift ice is represented as the moving ice present during the entire winter and spring, slightly shifted relative to the landfast ice (C in Fig. 8a). This is consistent with the findings of Swirad et

Table 1. Parameters describing polygons for separating ice types.

Parameter (values/units)	Meaning/calculation	Expected importance	Stage of workflow
Ice class (1 = moving; 2 = stationary)	Stationary ice is persistent in a given location for at least 15 d.		
Date (yyyy-mm-dd)	Extracted from the scene name	It determines whether the ice is in or outside the sea ice or landfast ice season (Table 2).	Temporal constraint on landfast ice; splitting moving ice
Surface area (m^2)	QGIS Add Geometry Attributes tool	The smallest ice polygons may be speckle or ships; landfast ice polygon size is partly controlled by the bay size.	Spatial constraint on landfast ice; splitting moving ice
Distance from the bays (m)	Zonal statistics (mean, min, max) on the distance raster (Fig. 6a); varies every year	Landfast ice occurs in the bays.	Spatial constraint on landfast ice (min, max)
Distance from the sea (m)	Zonal statistics (mean, min, max) on the distance raster (Fig. 6b); the same for the whole dataset	Only drift ice is expected in the open sea.	Splitting moving ice (min)
Distance from the land (m)	Zonal statistics (mean, min, max) on the distance raster (Fig. 6c); varies every year	Ice polygons adjacent to the land may be waves breaking (white water) and rocks and shallows exposed during the low tide.	Spatial constraint on landfast ice (min, max); splitting moving ice (mean)
Distance from the glacier fronts (m)	Zonal statistics (mean, min, max) on the distance raster (Fig. 6d); varies every year	Glacier ice is located close to the glacier fronts.	Splitting moving ice (max)
Distance from the Dunøysundet/Notting-hambukta (DN) area (m)	Zonal statistics (mean, min, max) on the distance raster (Fig. 6e); the same for the whole dataset	Glacier ice occurs far from the DN area.	Splitting moving ice (min)
Minimal ice class value in a 50 m buffer (0 = no ice; 1 = moving)	Zonal statistics (min) on the raster with stationary, moving, masked ice and no ice (open water and landmask)	If the minimal value is "1" the polygon is "moving ice" located inside a larger "stationary ice" polygon and should be classified as "landfast ice".	Spatial constraint on landfast ice

al. (2024a) who showed that the drift ice appeared on average 24 d before the landfast ice onset and was gone around 20 d before the end of the landfast ice season. During the seasons with low air temperatures (2012/2013, 2014/2015, 2019/2020 and 2021/2022) the persistence-based separation resulted in detecting stationary ice well-beyond the cumulative $\sim 140 \, km^2$ bay extent (D in Fig. 8a). A set of thresholds based on the familiarity with the study area and understanding of the physical processes was subsequently applied to improve the ice type separation.

First, the landfast ice was extracted. The stationary ice that was outside the landfast ice season (Table 2) was put into the moving ice class. Then, the stationary ice that either was not adjacent to the land or stretched far from the bays was re-classified as moving ice. The landfast ice was allowed 1.5 km from the bays as it was observed to exceed

Treskelodden and Traunpynten and surround Emoholmane islands. Small ($\leq 4 \, km^2$; dictated by the bay size) landfast ice polygons located no farther than 1.3 km from the land were also allowed at 5 to 9.5 km from the bays to encompass Hansbukta/Isbjørnhamna area and Gåshamna (for locations see Fig. 1). Moving ice fully surrounded by stationary ice was ascribed the landfast ice class. Figure 8b–c shows how the temporal and spatial thresholds helped delimit the landfast ice. During the cold seasons the temporal constraint still allowed the landfast ice to be present in the main basin and the open sea (E in Fig. 8b). The spatial constraint limited this effect but resulted in the entire polygon transition to the drift ice class (F in Fig. 8c). This was addressed later at the pixel level (last step in Fig. 3).

Subsequently, a set of thresholds described below was set to split the moving ice into drift ice and glacier ice. An ad-

Table 2. Timing and duration of the sea ice and landfast ice season in Hornsund from 2011–2023. The dates of onset and end of drift and landfast ice were defined visually from SAR imagery. The sea ice season is a period between the day with first drift ice inside the fjord and the landfast ice end, and the landfast ice season is a period between the onset and the end of landfast ice (Swirad et al., 2024a).

Season	First drift ice	Landfast ice onset	Last drift ice	Landfast ice end	Length of sea ice season (days)	Length of landfast ice season (days)
2011/2012	11 Dec	17 Feb	06 Jun	11 Jun	184	116
2012/2013	8 Feb	11 Feb	04 Jun	21 Jun	134	131
2013/2014	2 Jan	12 Jan	09 Apr	19 May	138	128
2014/2015	29 Dec	27 Jan	13 Jun	07 Jul	191	162
2015/2016	15 Feb	30 Mar	26 May	29 May	105	61
2016/2017	01 Mar	07 Mar	18 May	18 Jun	110	104
2017/2018	30 Dec	29 Jan	23 May	04 Jun	157	127
2018/2019	25 Jan	12 Feb	03 Jun	18 Jun	145	127
2019/2020	28 Oct	18 Dec	26 May	29 Jun	246	195
2020/2021	02 Feb	04 Feb	08 Jun	24 Jun	143	141
2021/2022	03 Dec	28 Dec	23 May	22 Jun	202	177
2022/2023	11 Feb	21 Feb	24 May	12 Jun	122	112
Average	11 Jan	4 Feb	26 May	16 Jun	156	132

ditional class called "uncertain" was imposed on all objects classified as ice in the binary classification (Swirad et al., 2023a, 2024a, b) which were not masked because of the radar shadows (Sect. 3.2.2) but did not fulfil the criteria to be classified as one of the three ice types. These locations may represent speckle noise resulting from low signal-to-noise ratio or from the atmospheric effect on backscatter variability but also ships, nearshore wave breaking (white water), or exposed rocks and shallows during low tide. The ice outside of the sea ice season was classified as glacier ice unless it was outside the fjord or was both > 3.5 km from the glacier front and focused along the coast (Table 2). The first condition was based on the field observations that the plumes of produced ice melangé, brash ice, growlers and bergy bits get dispersed and melt when still in the fjord while icebergs are rare in Hornsund and tend to be pushed nearshore and get anchored to the sea bottom rather than drift away to the open sea. The second condition is based on the observation that glacier ice persists nearshore close to the glacier fronts while the high backscatter values along the coast far from the glacier fronts likely represent white water and exposed rocks. Notably, the 100 m buffer around the land mask applied before running the segmentation algorithm (Sect. 3.1.1) made it impossible to detect the real ice accumulated at the shore.

During the sea ice season, the moving ice was considered drift ice. The motivation for this decision was the fact that there exists a high daily to weekly variability in drift ice distribution as well as the type of the drift ice which includes the pack ice ranging from grey ice (10–15 cm) to thick first-year ice (< 2 m) and in situ ice broken from the landfast ice (Swirad et al., 2024a). Drift ice may therefore be distributed throughout the study area and have a full range of ice polygon morphology. Finally, drift ice was allowed outside of the sea ice season if it was located in the open sea and was at

least 1 km^2. The sea ice season over the Barents Sea is longer than that of Hornsund and pack ice is observed sporadically in the southwestern part of the study area; usually it happens in late autumn – early winter before the sea ice season in Hornsund starts, but may happen earlier too with the high sea ice concentration in the fjord e.g. in August 2015. Ignoring the small polygons decreases the chance of misclassifying speckle noise, ships, white water and exposed rocks as drift ice.

3.2.4 Pixel-based refinement

Finally, the different ice type polygons and no ice zones were rasterized back into the maps with the extent and resolution of the original binary maps. Pixel values through time were used to automatically re-classify drift ice into landfast ice in bays in the periods of high sea ice coverage over the entire fjord (Fig. 8e). This means that if a pixel was ascribed "landfast ice" class, then "drift ice" and then "landfast ice" again, it was considered "landfast" throughout. Table 3 contains the information on the changes of spatial extent of different ice types at various stages of the workflow. The ice type maps were visually inspected.

3.3 Environmental datasets

Mean daily air temperature for the period 1 July 2011 to 30 June 2023 derived from 3-hourly automatic measurements with Vaisala HMP45D and HMP155 probes at the PPS Hornsund were obtained from Wawrzyniak and Osuch (2020) and the PPS archive (https://monitoring-hornsund.igf.edu.pl/index.php/login, last access: 21 July 2025). The probes are located in the vicinity of the main station building, ca. 200 m from the shore, at an elevation of 2 m a.g.l., which is ∼ 12 m a.s.l.

Table 3. Average spatial extent (km^2) of the ice types at various stages of the workflow.

Stage	Stationary	Moving	Landfast	Drift	Glacier	Uncertain	Masked
Before thresholding	46.20	37.31	–	–	–	–	1.83
Temporal constraint on landfast ice	–	38.00	45.51	–	–	–	1.83
Spatial constraint on landfast ice	–	57.92	25.59	–	–	–	1.83
Split of moving ice	–	–	25.59	49.49	7.21	1.22	1.83
Pixel-based refinement of drift and landfast ice	–	–	30.19	44.89	7.21	1.22	1.83
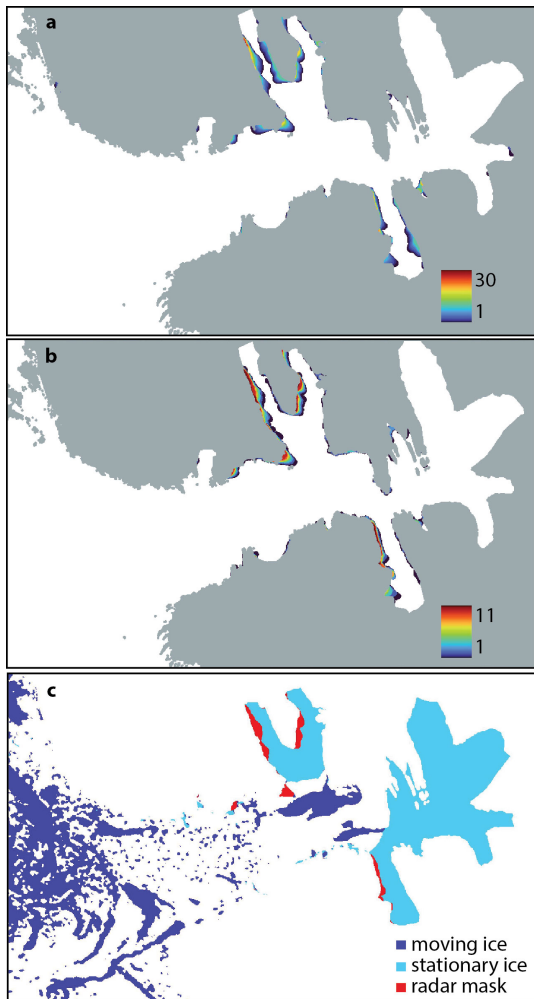
Figure 5. Radar shadow masks: the number of orbits with a shadowed area for **(a)** RADARSAT-2, **(b)** Sentinel-1, **(c)** an example radar mask applied on the 29 April 2013 split scene.

Hourly water temperature from the sea bottom moorings were collected as part of the LONGHORN oceanographic monitoring of the PPS (https://dataportal.igf.edu.pl/dataset/temp_sal_one_hour_averaged_mooring_data; last access: 21 July 2025). The data from eight deployments spanning 1 June 2014 to 9 June 2024 were used that included nearshore (10–23 m depth) locations in the north-western Hornsund (Hans-

bukta, Isbjørnhamna and Veslebogen; Fig. 1). The measurements were taken with HOBO Water Temp Pro v2 (U22-001), RBRsolo T and RBRconcerto CTD (Table 4). Daily water temperature was calculated by averaging over the hourly data.

Finally, the landmasks (Sect. 3.1.1) were used to calculate the gain of fjord surface area and approximate tidewater glacier front retreat.

4 Results

Ice type maps at 50 m resolution spanning from 2 January 2012 to 29 June 2023 ($n = 2639$; ~ 1.59 d map^{-1}) include seven classes: open water, drift ice, landfast ice, glacier ice, uncertain, masked and landmask (Swirad, 2025). The uncertain and masked classes were classified as ice in the binary maps (Swirad et al., 2023a, 2024b) but were disregarded from the main ice type classes because of the radar shadows (masked class) or not fulfilling the ice type criteria and likely representing speckle, white water, ships etc (uncertain class).

Averaged over the 11.5-year study period, 53 % of the ice was classified as drift, 35 % as landfast, 8.5 % as glacier, 2.1 % as masked and 1.4 % as uncertain (Table 3). The abundance and location of the different ice types varied during the monitoring period. Drift ice had the largest extent that included the open sea, DN area, main basin and the bays. It reached the maximum average 28 % presence in the DN area. Landfast ice concentrated in the bays with the most frequent appearance (up to 33 %) in the inner-most parts of Samarinvågen and Brepollen. Glacier ice persisted in bays of tidewater glaciers with the highest recurrence (16 %) in Vestre Burgerbukta where Paierlbreen is located. The uncertain class dominated in the open Greenland Sea (speckle) and nearshore (white water, tidal zone). Masked areas mostly covered western parts of Burgerbukta and Samarinvågen characterised by steep mountain slopes (Fig. 9).

The study period included 12 sea ice seasons (2011/2012–2022/2023) and 11 summer periods (2012–2022). The ice pack from the Barent Sea appeared between 28 October (2019/2020) and 1 March (2016/2017) with an average on 11 January. The landfast ice season started between 18 December (2019/2020) and 30 March (2015/2016) with an average on 4 February. The length of sea ice seasons varied from 105 d in 1015/1016 to 246 d in 2019/2020 (average 156 d).

Table 4. Water temperature data used in the study.

LONGHORN ID	Latitude (° N)	Longitude (° E)	Depth (m)	Start (dd/mm/yyyy)	End (dd/mm/yyyy)	Days	Instrument
T01	77.0009	15.6246	23	01/06/2014	21/05/2015	355	HOBO Water Temp Pro v2 (U22-001)
T03	77.0031	15.6298	22	10/06/2015	26/06/2016	383	HOBO Water Temp Pro v2 (U22-001)
T06	76.9977	15.5605	10	13/06/2016	23/05/2017	345	RBRsolo T
T07	76.9977	15.5599	10	02/06/2017	22/05/2018	355	RBRsolo T
CTD03	76.9951	15.4881	17	05/06/2018	09/06/2019	370	RBRconcerto CTD
CTD04	76.9952	15.4894	16	25/06/2019	05/03/2021	620	RBRconcerto CTD
CTD07	77.0029	15.5843	11	08/09/2022	02/06/2023	268	RBRconcerto CTD
CTD09	76.9955	15.5665	16	11/06/2023	09/06/2024	365	RBRconcerto CTD

The landfast ice season varied from 61 d in 2015/2016 to 195 d in 2019/2020 (average 132 d) (Table 2). The least icy sea ice seasons were 2013/2014, 2011/2012 and 2015/2016, while the iciest were 2012/2013, 2019/2020 and 2021/2022 and 2014/2015 (Fig. 10).

On average, sea ice (drift and landfast ice) covered 40 % of the fjord area during the sea ice season with the highest coverage in 2012/2013, 2019/2020, 2021/2022 and 2014/2015, and the lowest in 2013/2014 and 2011/2012. The landfast ice covered on average 26 % of the fjord area during the landfast ice season, but it ranged from 3.1 % in 2013/2014 and 4.6 % in 2011/2012 to 40 % in 2019/2020 and 39 % in 2021/2022. Glacier ice coverage during the sea-ice-free seasons averaged 4.1 % and ranged from 3.7 % in 2020 to 5.2 % in 2015 (Table 5). The seasons 2011/2012 and 2013/2014 were characterised by the lowest mean coverage and smallest spatial extent of the landfast ice that did not encompass all legs of the bays (Fig. 11). Glacier ice was consistently present in Burgerbukta and Samarinvågen but for Hansbreen and the Brepollen glaciers it was more diverse from year to year (Fig. 12).

The Mann–Kendall test (Mann, 1945; Kendall, 1970) was used to verify whether an interannual trend existed in season duration and ice coverage over the analysed 11.5 years. For all parameters the trend was positive and insignificant with the τ and p values of 0.09 and 0.73 for the length of sea ice season, 0.17 and 0.49 for the length of landfast ice season, 0.06 and 0.84 for the drift ice coverage during the sea ice season, and 0.27 and 0.24 for the landfast ice coverage during the landfast ice season.

The ice type distribution also varied seasonally. Drift ice had the highest coverage in March (25 %) with up to 53 % in 2012/2013, 47 % in 2019/2020 and 46 % in 2021/2022. Landfast ice had the highest coverage in April (33 %), but in 2019/2020 the coverage over 40 % persisted for five and in 2021/2022 for four months. The highest coverage of glacier ice characterised October (7.9 %) (Fig. 13).

The timeseries of air and water temperatures show a clear seasonal pattern with higher temperatures in summer and lower in winter. The mean air temperatures in summer months (July–September) were relatively similar from year to year (4.0 to 5.4 °C), while the largest variability charac-

terised winter (January–March; −12.8 to −3.0 °C) and autumn (October–December; −5.8 to 0 °C), followed by spring (April–June; −2.6 to −0.1 °C). The coldest seasons were 2019/2020 and 2012/2013. Cold autumns generally did not associate with cold winters, except for the coldest 2019/2020. Water temperatures were lower than air temperatures during the summer months, and higher during the rest of the year. The 2019/2020 season was the only one with negative mean autumn water temperatures, while 2019/2020 and 2013/2014 had −1.9 °C mean in winter (Fig. 14; Table 6).

The yearly updated landmasks reflected the result of glacier retreat on study area (fjord water) increase over the monitored 12 seasons, with a total increase of 29.76 km^2, equivalent to 11 % relative to 2011 or 2.48 km^2 yr^{-1}. The largest area gain was for Brepollen (16.87 km^2; 21 %) but in Samarinvågen which gained three times less area, the Samarinbreen retreat contributed to a 39 % gain. The main basin experienced the lowest area increase (2.4 km^2; 1.6 %) due to the Hansbreen retreat. The gain was not uniform through time with the highest fjord area increase in 2013/2014 (5.87 km^2), 2022/2023 (4.81 km^2) and 2016/2017 (4.55 km^2) and the lowest in 2015/2016 (0.35 km^2), 2019/20 (0.65 km^2) and 2018/2019 (1.28 km^2) (Table 7).

The length of sea and landfast ice seasons, and the coverage of sea, drift and landfast ice were positively correlated with one another with the highest correlation of the length of sea ice seasons versus the length of landfast ice season (Pearson correlation coefficient, PCC = 0.95, $p < 0.05$) and of the sea ice coverage versus landfast ice coverage (PCC = 0.92, $p < 0.05$). The sea ice parameters did not correlate with the glacier ice coverage in the preceding sea-ice-free period. The length of the ice season was negatively correlated with the air and water temperatures with the strongest correlation between the water temperature in winter months and the length of the landfast ice season (PCC = −0.94, $p < 0.05$) and the sea ice season (PCC = −0.89, $p < 0.05$). However, the winter air rather than water temperature was more important for the coverage of sea ice (PCC = −0.87, $p < 0.05$), landfast ice (PCC = −0.86, $p < 0.05$) and drift ice (PCC = −0.78, $p < 0.05$). The air and water temperatures themselves were usually non-correlated except for a strong positive correlation in autumn (PCC = 0.92, $p < 0.05$) and a moderate cor-

Table 5. Average seasonal ice type extent and coverage in Hornsund from 2011–2023. For the dates see Table 2.

Season	Sea ice (drift + landfast) extent during the sea ice season (km^2)	Sea ice (drift + landfast) ice coverage during the sea ice season (%)	Drift ice extent during the sea ice season (km^2)	Drift ice coverage during the sea ice season (%)	Landfast ice extent during the landfast ice season (km^2)	Landfast ice extent during the landfast ice season (%)	Glacier ice extent during the preceding sea-ice-free season (km^2)	Glacier ice coverage during the preceding sea-ice-free season (%)
2011/2012	47.01	17.07	38.17	13.86	12.55	4.56	–	–
2012/2013	180.17	64.75	72.11	25.92	98.62	35.45	11.76	4.23
2013/2014	37.80	13.48	28.53	10.18	8.63	3.08	13.88	4.95
2014/2015	144.64	50.53	56.21	19.64	99.02	34.59	13.92	4.87
2015/2016	60.60	21.01	26.93	9.33	59.91	20.77	15.12	5.24
2016/2017	131.66	45.59	49.62	17.18	83.52	28.92	12.45	4.31
2017/2018	84.99	28.97	39.82	13.57	54.45	18.56	11.64	3.97
2018/2019	120.11	40.75	31.36	10.64	98.64	33.46	13.42	4.55
2019/2020	173.11	58.47	77.68	26.24	118.31	39.96	14.90	5.03
2020/2021	121.38	40.91	36.30	12.24	80.03	26.97	11.04	3.72
2021/2022	158.70	53.10	65.21	21.82	115.31	38.58	13.51	4.52
2022/2023	145.79	48.53	50.85	16.93	97.09	32.32	12.35	4.11
Average	117.16	40.26	47.73	16.46	77.17	26.43	12.00	4.13

Table 6. Seasonal variability in air and water temperature in Hornsund from 2011–2023.

Season	Mean air temperature in Jul–Sep (°C)	Mean air temperature in Oct–Dec (°C)	Mean air temperature in Jan–Mar (°C)	Mean air temperature in Apr–Jun (°C)	Mean water temperature in Jul–Sep (°C)	Mean water temperature in Oct–Dec (°C)	Mean water temperature in Jan–Mar (°C)	Mean water temperature in Apr–Jun (°C)
2011/2012	4.06	−3.09	−2.99	−2.54	–	–	–	–
2012/2013	4.07	−3.08	−9.46	−2.45	–	–	–	–
2013/2014	5.43	−4.93	−3.56	−1.96	–	–	–	–
2014/2015	4.31	−4.10	−7.47	−1.39	4.24	0.63	−1.92	−1.21
2015/2016	4.32	−2.41	−3.93	−0.07	2.14	0.29	−0.59	−0.15
2016/2017	5.06	−0.04	−7.53	−2.60	3.47	2.34	−0.89	−0.45
2017/2018	5.13	−1.54	−6.27	−1.03	3.69	1.21	−1.57	−0.14
2018/2019	4.01	−2.24	−8.95	−0.40	3.26	1.24	−1.44	0.20
2019/2020	4.19	−5.83	−12.82	−1.73	3.49	−0.71	−1.90	−0.65
2020/2021	4.79	−2.33	−6.34	−1.81	3.47	1.02	−1.28	–
2021/2022	4.26	−4.57	−8.47	−2.38	–	–	–	–
2022/2023	4.87	−2.28	−6.25	−0.44	–	1.10	−1.23	−0.09
Average	4.54	−3.04	−7.00	−1.57	3.39	0.89	−1.35	−0.35

relation of autumn and winter air temperatures versus winter water temperatures (PCC = 0.67, $p < 0.05$). Glacier ice coverage had a negative correlation with summer air and autumn water temperatures (PCC = −0.75 and −0.72, respectively, $p < 0.05$). Fjord area gain was correlated positively to autumn water temperatures (PCC = 0.8, $p < 0.05$) and negatively to spring air temperatures (PCC = −0.78, $p < 0.05$) (Fig. 15).

5 Discussion

Automated fjord ice mapping, and more widely nearshore ice mapping has been rarely attempted likely due to the challenges related to the mixed land/water pixels, presence of islands, rock and shallows, wave breaking and impact of topography on sea-state and radar shadowing. In addition, the often sheltered areas present in Hornsund result in level sea ice formation and a lack of textural features often used for sea ice classification (e.g., Lohse et al., 2019; Guo et al., 2025). Moreover, the level ice and an early ice formation have at times low signal-to-noise ratio (SNR), making accurate ice

type classification challenging (Park et al., 2020). Here we followed the method of binary ice/open water mapping developed by Cristea et al. (2020) for open ocean, and adapted to the Svalbard fjords by Johansson et al. (2020) and to Hornsund specifically by Swirad et al. (2024a). Limitations of the method were discussed by Swirad et al. (2024a).

To our knowledge, this is the first attempt to automatically separate ice types in a fjord. Splitting ice types using only radar backscatter sigma nought values and the incidence angle is challenging given similar backscatter values for the various ice types, and the varying wind conditions due to the topography and coastal areas. It might be possible to use the backscatter values to investigate properties of the sea ice affecting the backscatter, such as early ice thickness growth, surface roughness, changes to the ice snow cover due to melting and wind effects. In situ observations of snow cover made by the PPS Hornsund crew, as well as the weather station and the ocean mooring system enable robust assessments of such changes. Moreover, single-pass InSAR can be used to identify the landfast ice extent provided high interferometric coherence and sufficient SNR values which partially depends

Table 7. Surface area of Hornsund and its parts (km^2) as delimited in Fig. 1 and the annual fjord area gain based on the 2011–2023 land masks. The landmasks were based on NPI (2014), updated annually with a SAR image from 1 July (or the first available thereafter) and a 100 m buffer was added along the coast to exclude the tidal zone.

Land mask	Hornsund	Main basin	Burgerbukta	Brepollen	Samarinvagen	All bays	Annual gain
2011	275.46	150.74	29.81	81.91	13.01	124.73	–
2012	278.23	150.90	30.45	83.49	13.40	127.34	2.77
2013	280.38	151.09	30.69	84.98	13.62	129.29	2.15
2014	286.25	151.86	31.50	88.57	14.33	134.39	5.87
2015	288.47	151.69	32.02	90.05	14.71	136.79	2.23
2016	288.82	151.68	31.87	90.39	14.88	137.14	0.35
2017	293.37	151.93	32.96	92.72	15.76	141.44	4.55
2018	294.78	152.07	33.20	93.36	16.17	142.72	1.41
2019	296.07	152.11	33.15	94.16	16.64	143.95	1.28
2020	296.72	152.07	33.13	94.66	16.86	144.65	0.65
2021	298.84	152.24	33.85	95.47	17.28	146.60	2.12
2022	300.40	152.57	34.14	95.99	17.71	147.83	1.57
2023	305.42	153.17	35.26	98.86	18.13	152.25	5.02
Average	291.02	151.86	32.46	91.12	15.58	139.16	2.50

on the ice thickness due to the low SNR in early ice formation stages and low backscatter values for level ice with low amount of textural features (Dierking et al., 2017).

Drift ice algorithms often rely on feature tracking (Muckenhuber and Sandven, 2017; Korosov and Rampal, 2017; Gao et al., 2025) to determine the drift between two subsequent SAR images. The landfast ice formed within the study area typically has a low degree of textural features, and the drift ice originating from the landfast ice likely has floe size smaller than the pixel size (50 m) and as such using drift retrievals for the ice formed within the fjord is challenging. Drift retrievals may be used to capture the ice entering the fjord system from the Greenland Sea, though the method may be challenging if the drift ice gets incorporated into the landfast ice areas.

The sea ice within the Hornsund basin is predominantly first-year ice that forms under calm conditions as landfast sea ice, and as such has an inherently low textural variability (Kim et al., 2020) and for part of the season has low backscatter due to the new ice formation stage (Liu et al., 2025). Textural information is an integral part in many existing sea ice type classification methods (Park et al., 2020), and level landfast ice is known to be challenging to accurately classify with existing sea ice classification methods (Kim et al., 2020; Wang et al., 2023; Zhu et al., 2025). Hence, inherent ambiguities in the SAR images between different ice types may transfer inaccuracies in sea ice type classification to the accuracy in separation between sea ice and open water. Although they are similar in backscatter values, the types of ice can be separable by their persistence through time, location, timing, size and shape.

Therefore, we believe that in order to divide fjord ice into landfast, drift and glacier ice types, the threshold-based method described in here is the most suitable. The method

is simple, computationally cheap and it is based on the familiarity with the study site and understanding of ice processes. It uses a set of thresholds including persistence in time, timing, location and ice polygon size. In our approach we opted for fewer thresholds that can divide relatively large portions of ice, which makes some situations impossible to resolve. For instance, glacier ice inside the sea ice season is always classified as drift or landfast ice. Sea ice formation around water-cooling glacier ice is undetectable. The landfast ice edge fluctuation area is likely mapped as drift ice, because of alternating "ice" and "open water" labels reappearing in those pixels. However, most of these situations are challenging to resolve with available SAR imagery anyway, and an extensive field experiment is needed to better quantify those processes. Optical imagery can resolve some of these challenges (Makhotina et al., 2025), though the area is often cloud covered and the resolution needed to fully resolve such changes offered by, e.g., Planet Scope images are not regularly acquired over the area. Landsat and Sentinel-2 images are possible to use though the revisit times of 16 d (8 d if Landat-8 and -9 are combined) and 5 d, respectively, prevent from reliably resolve of landfast changes. Additionally, optical images do not cover the area in the polar night, and few are available from November to February, limiting the possibility of using optical images to capture the drift ice start up as well as the initial landfast ice formation period.

It is challenging to provide an accuracy measure for the applied method, particularly for potential errors from the binary classification that may propagate to the ice type mapping. Time series of ice type extent (Fig. 10) and maps of coverage (Figs. 11–12) appear reasonable, but were made with user-defined conditions. A small portion of ice extent (3.5 %) was classified as "masked" or "uncertain". This value can be used as an uncertainty measure for the method, since some
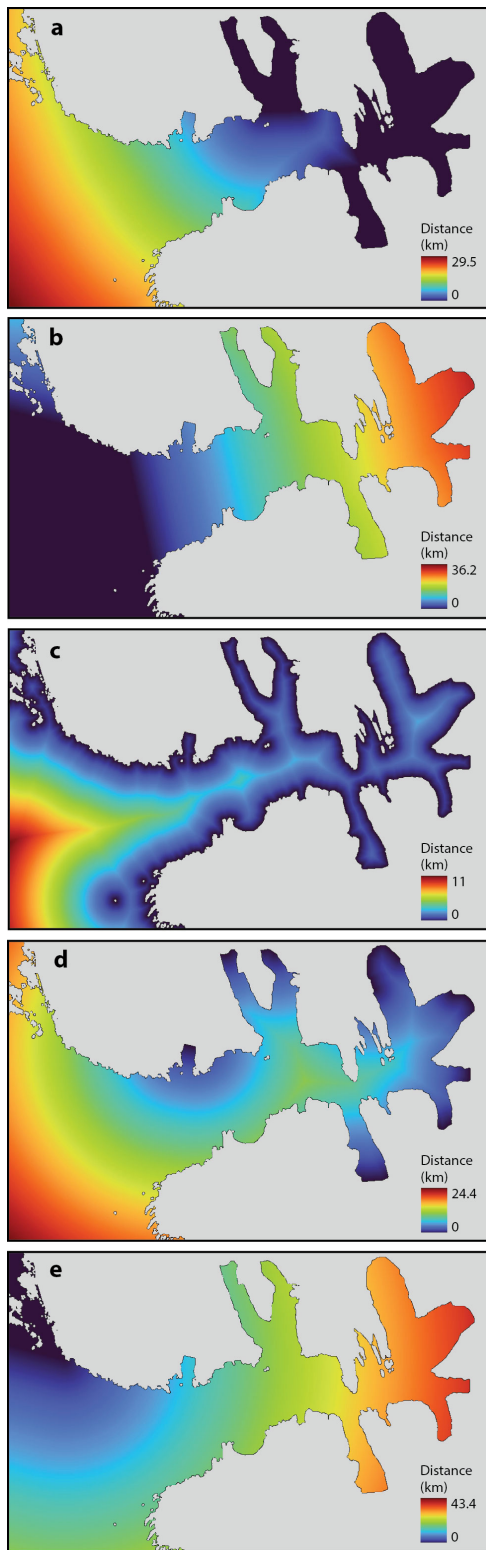
Figure 6. Maps of the aerial distance from: **(a)** the bays, **(b)** the sea, **(c)** the land, **(d)** the glacier fronts, and **(e)** the Dunøysundet/Nottinghambukta (DN) area as delimited in Fig. 1 for July 2018–June 2019.
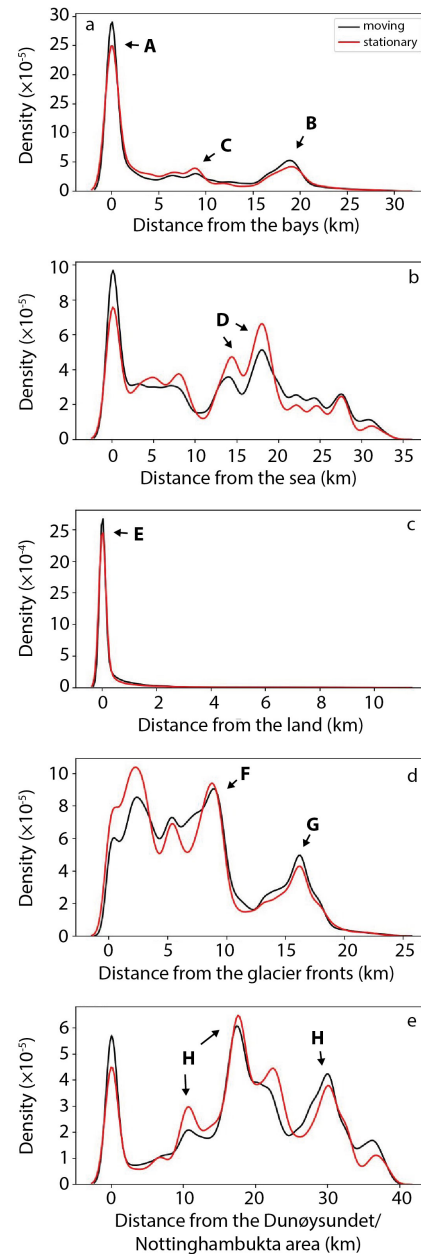

Figure 7. Kernel density distribution of the mean distance from **(a)** the bays, **(b)** the sea, **(c)** the land, **(d)** the glacier fronts, and **(e)** the Dunøysundet/Nottinghambukta (DN) area for the moving and stationary ice polygons in 2012–2023.

areas covered by these two classes can indeed include landfast, drift or glacier ice, while others are likely speckle noise, radar shadow, tidal effect, etc. over ice-free water.

The method will need calibration if used in other fjords with different size, shape, bathymetry and hydrography. For instance, using aerial distances from bays, sea, land, glacier fronts and DN area rather than shortest path on water was sufficient in Hornsund given its morphology but may be erroneous in different fjords. Following are some particular fea-
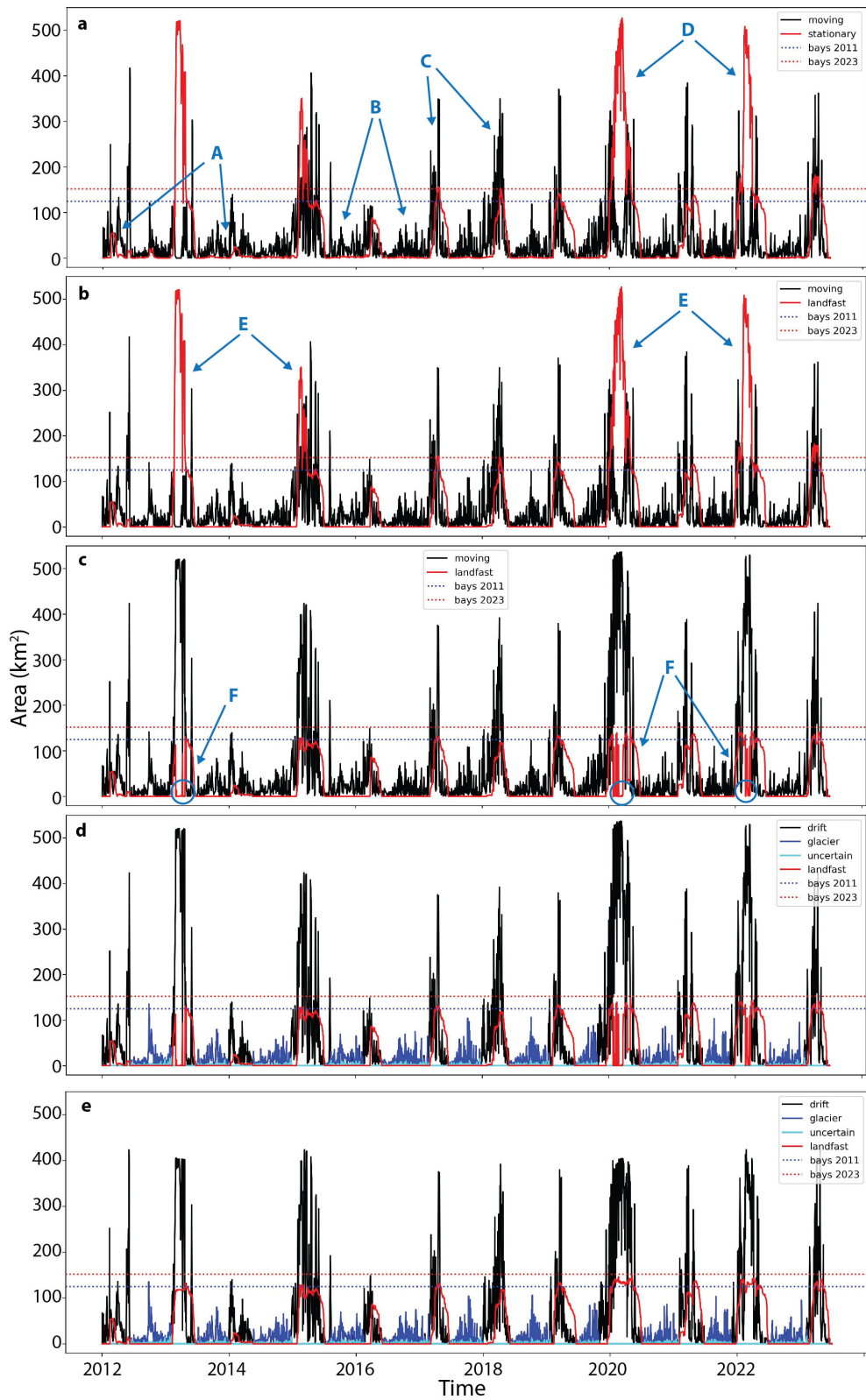
Figure 8. Time series of ice classes and types in Hornsund in 2012–2023 at different stages of the workflow (Fig. 3): **(a)** moving and stationary ice based on the 15 d persistence split, **(b)** temporal constraint on the landfast ice, **(c)** spatial constraint on the landfast ice, **(d)** split of moving ice into drift and glacier ice, **(e)** pixel-based refinement of drift and landfast ice. Note the bay increase over 12 years as the glaciers retreat.
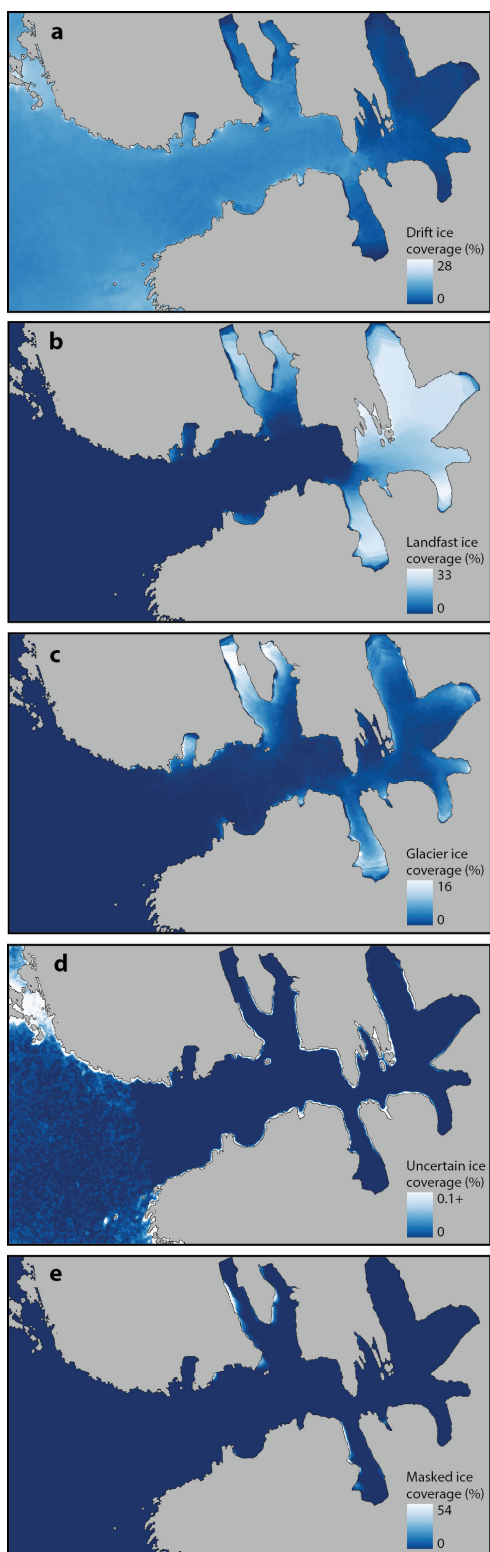
Figure 9. Average ice presence in Hornsund between 2 January 2012 and 29 June 2023: **(a)** drift ice, **(b)** landfast ice, **(c)** glacier ice, **(d)** uncertain ice, and **(e)** masked ice.

tures of Hornsund that dictated values of calibrated parameters. The cold Sørkapp Current precludes warm Atlantic Water entering the fjord and brings cold and fresh water masses as well as pack ice from Storfjorden and the Barents Sea. This itself makes Hornsund hydrography very different from more northern fjords such as Bellsund or Isfjorden. The Barents Sea area experiences one of the highest sea ice declines in the Arctic which affects drift ice presence in the Hornsund area. Since the "regime shift" in 2005, the pack ice at the entrance to the fjord has appeared episodically (Herman et al., 2025). On the other hand, the tidewater glaciers of Hornsund retreat is around twice as fast as elsewhere in Svalbard (Błaszczyk et al., 2013), has resulted in increasing fjord area (11 % over 12 years; Table 7) and thus contributes glacier ice to the fjord. Retreating Hornbreen (Brepollen) and Hambergbreen (Storfjorden) are expected to cause the transition of Hornsund from a fjord to a straight in 2055–2065 (Grabiec et al., 2018).

Changes in the ice conditions impact the range of aspects of the fjord environments including coastal hazards. Episodic presence of pack ice at the entrance to the fjord, coupled with increasing frequency and duration of storms over the Greenland Sea (Wojtysiak et al., 2018), make more energetic waves enter the fjord more often. Zagórski et al. (2015) observed an increased rate of shoreline retreat in Isbjørnhamna, the bay at which the PPS Hornsund is located, in 1990–2011 relative to 1960–1990. The authors ascribed it to the intensification of storms in the periods of positive air temperature anomalies and lack of sea ice cover. Our results suggest that the storm waves occurring before January/February (average start of sea ice and landfast ice seasons) may have direct access to the shore. However, Herman et al. (2025) observed the shift of maximal wave energy from late autumn (November–December) in 1979–2005 to winter (December–March) in 2006–2023 caused by the decline in pack ice. Increased nearshore wave energy translates into higher wave runup, and consequently a risk of coastal flooding and erosion (Casas-Prat and Wang, 2020). These relationships are yet to be empirically found for Hornsund. An important factor limiting wave action on the beach is ice present at the shore which in Hornsund includes both glacier ice and shore ice (ice foot), a band of ice of diverse origin (glacier and sea ice, frozen swash and splash, compacted snow) cemented to the shore (Rodzik and Zagórski, 2009). Our analyses did not include ice on the shore due to the 100 m buffer along the coastline. Field observations suggest that shore ice is present annually. It has recently rarely formed before January, though it persists until May–June. Future efforts should include monitoring and modelling of nearshore wave transformation and wave energy delivery to the beach.

This study provides 11.5 years of near-daily maps of ice types which can be used to (i) assess the probability of given ice conditions in specific time periods, e.g. for planning boat or snowmobile operations, and (ii) find a long-term pattern in changing ice conditions in response to the climate
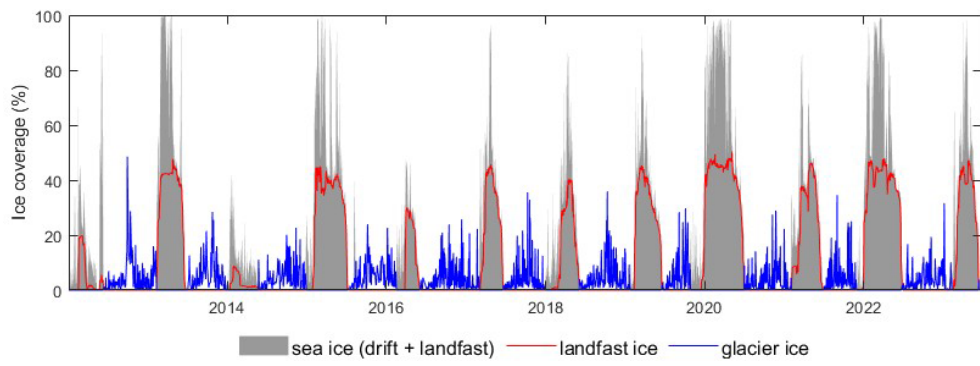
**Figure 10.** Time series of fjord ice coverage in Hornsund from 2012–2023.
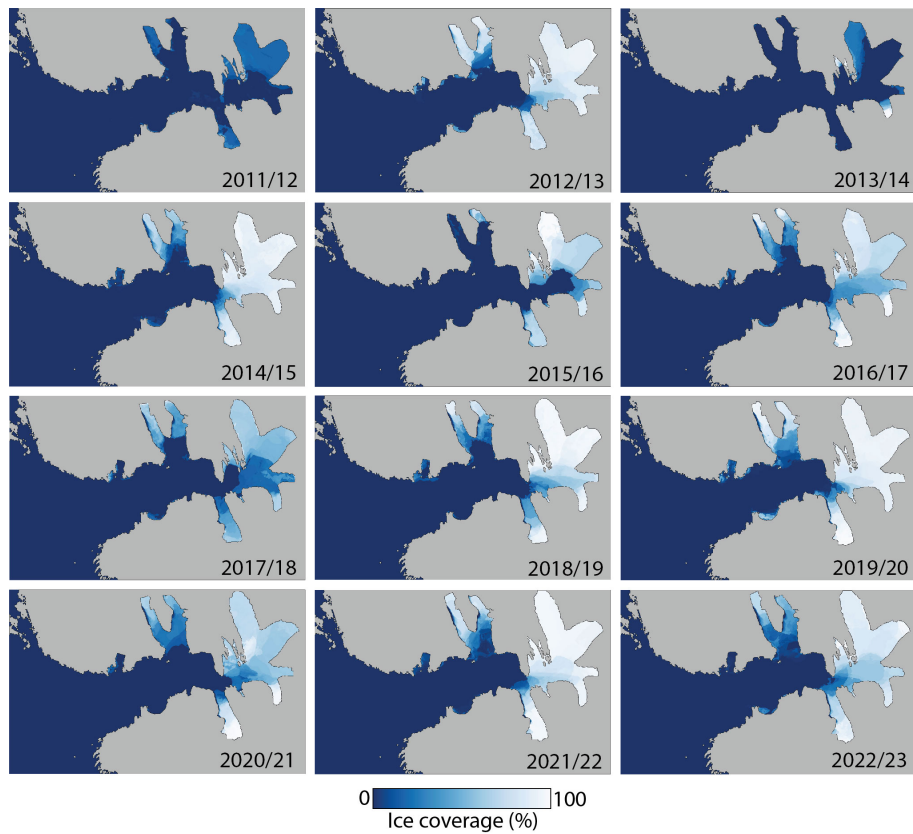
Figure 11. Average landfast ice presence in Hornsund for the landfast ice seasons 2011/2012 to 2022/2023 (for dates see Table 2).

change. However, the Mann–Kendall test showed no interannual trend in the length of the sea ice and landfast ice seasons or in the coverage of drift, landfast and glacier ice over the study time period. We speculate that a long-term trend could be visible if the pre-2005 regime shift period was incorporated (Muckenhuber et al., 2016; Herman et al., 2025). There is a great interannual variability in all ice type extents and icy years occur both earlier (2012/2013) and later (2019/2020 and 2021/2022) in the monitoring period. Also seasonally, there is no shift in the peak extent of different ice types. Therefore, it appears that predictions of ice conditions in a specific period can only be made by observing meteorological conditions leading to it, such as autumn air or winter water temperature.

Pair-wise correlation between ice and environmental parameters shows a few interesting trends (Fig. 15). As the date range of the end of sea ice season (same date as landfast ice season) is relatively limited (~ 1.5 months), the length of the season is mostly dictated by the beginning of the season which ranges by up to four months for the sea ice and three months for the landfast ice season. The strong relationship between the length of sea and landfast ice seasons may sug-
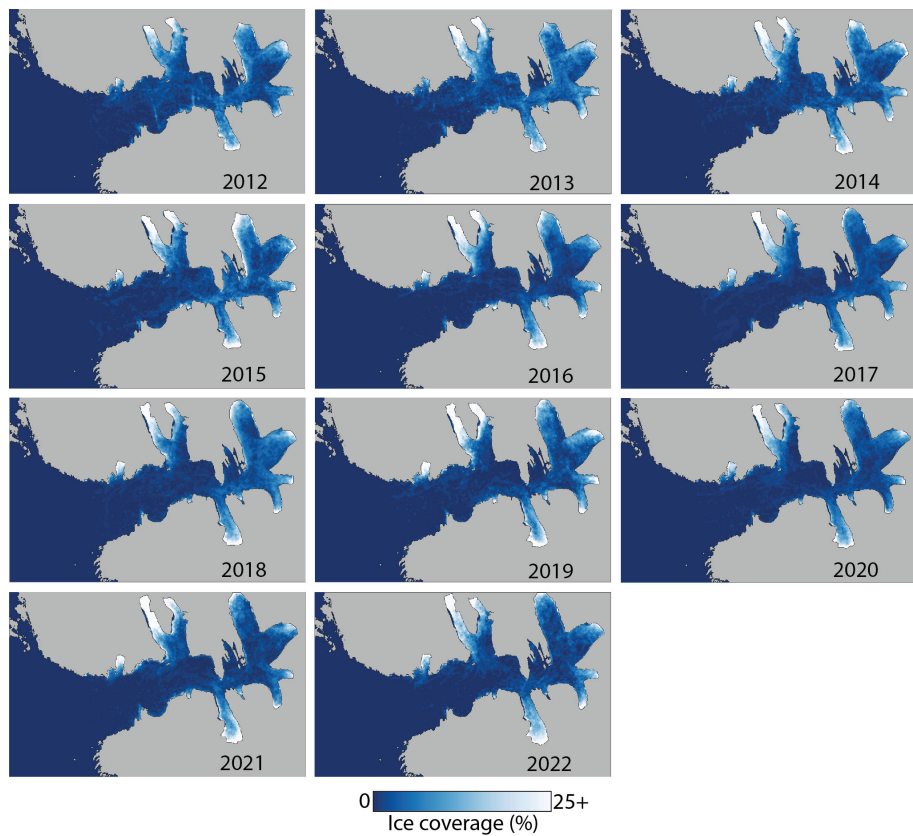
Figure 12. Average glacier ice presence in Hornsund for the sea-ice-free seasons 2012 to 2022 (for dates see Table 2).
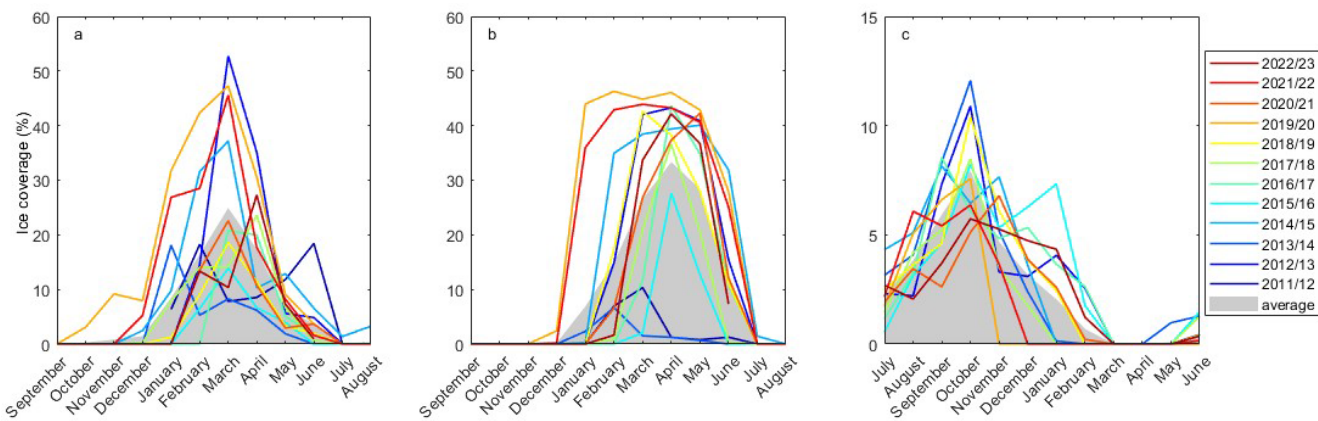
Figure 13. Mean monthly extent of fjord ice in Hornsund from 2012–2023: **(a)** drift ice, **(b)** landfast ice, **(c)** glacier ice. Note that both axes differ for the glacier ice.

gest that earlier arrival of the pack ice from the Barents Sea causes an earlier formation of landfast ice, which could imply one or both situations: the drift ice is anchored to the land forming a core of the landfast ice or the presence of drift ice creates favourable conditions for the landfast ice to form, e.g. by decreasing water temperatures or preventing waves from entering the inner parts of the fjord. The statistically significant negative correlation between winter water temperature

and the length of ice season could suggest the pack ice lowering water temperature but it may also be a second order effect of local weather conditions since winter water temperature is dependent on autumn air temperature (lag due to slower heat exchange of the water). If so, the monitoring of the air temperature at PPS Hornsund in autumn could allow an estimation of when the landfast ice forms. Our data suggest that a 1 °C decrease in the average October–December
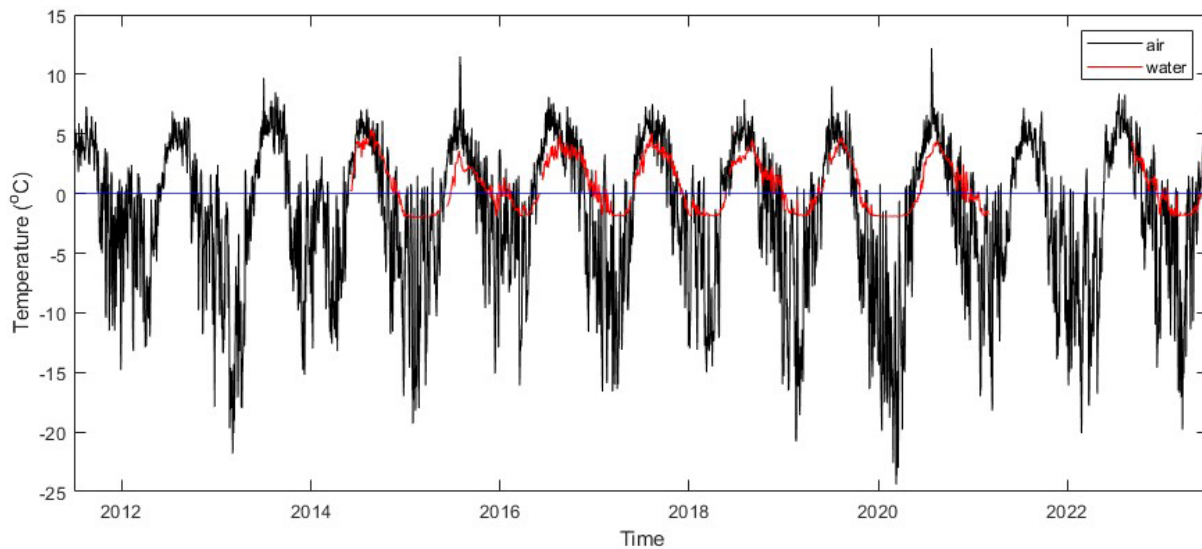
Figure 14. Time series of daily air and water temperature in Hornsund between 1 July 2011 and 30 June 2023.

air temperature results in 19 d longer sea ice season (linear regression $R^2 = 0.53$).

Here we only investigate water temperature at the three-month (season) scale. However, the in situ sea ice formation by water freezing is a complex process where not only temperature but also salinity, wind conditions and sea state are important (Lubin and Massom, 2006; Wang et al., 2021). The freezing point of seawater decreases with increasing salinity (Roquet et al., 2022). Thus, saline Atlantic Water requires stronger cooling to reach freezing compared to fresher Arctic Water. Consequently, the inflow of saline Atlantic Water versus fresh Arctic Water into the fjord in summer/autumn may be critical for the formation of landfast ice in winter (Arntsen et al., 2019). Continued hydrographic monitoring and higher-resolution observations of ice formation than those presented in this study are essential to improve our understanding of sea ice–ocean interactions in Hornsund.

The negative relationship between winter air temperature and sea ice coverage is intuitive, but two interesting nuances should be noted. Firstly, is it air and not water temperature that controls the coverage which may be explained by the fact that further decrease of water temperature leads to more in situ freezing so water temperatures below $-1.9\,°C$ cannot be recorded and linked to the coverage. Secondly, stronger correlation exists between winter air temperature and the sea ice coverage, and between winter air temperature and the landfast ice coverage (on average 66 % contributor to all sea ice) than between winter air temperature and the drift ice coverage which supports the hypothesis that drift ice is less dependent on local conditions than the landfast ice, being partly shaped by ice conditions in Eastern Svalbard as well as currents and winds outside Hornsund.

The statistically significant negative correlation of glacier ice coverage and summer air and autumn water tempera-

ture supports that during colder summers, ice produced from calving does not melt that quickly and remain on the fjord waters. The positive correlation of fjord area gain with autumn water temperature further points to the intensification of glacier calving in this period, while the negative correlation with spring air temperatures may show the periodic glacier front advance (Błaszczyk et al., 2013).

6 Conclusions

RADARSAT-2 imagery was used to extend an existing dataset of binary ice/open water maps in Hornsund fjord, Svalbard back in time. Subsequently, a 11.5-year archive of the binary maps at 50 m resolution was used to separate fjord ice into drift, landfast and glacier ice. The separation utilised a set of thresholds based on the familiarity with the study area and ice processes. The processing steps included (i) pixel-based splitting of the ice into stationary and moving classes using the 15 d persistence criterion, (ii) masking radar shadows, (iii) polygon-based classification into landfast, drift and glacier ice, and an uncertain ice class, and (iv) pixel-based refinement of drift and landfast ice.

In the result, a set of 2639 ice type maps was created for the 1 February 2012 to 29 June 2023 period with an average frequency of 1.59 d. These were used to characterize the spatial and temporal (seasonal and interannual) distribution of the ice types, and relate them to environmental conditions (air and water temperature, glacier front retreat).

Overall, 53 % of the ice was classified as drift, 35 % as landfast, 8.5 % as glacier, 2.1 % as masked and 1.4 % as uncertain ice type. There was a great variability in the length of sea ice season (105–246 d) and landfast ice season (61–195 d) as well as in the coverage of drift ice (9.3 %–
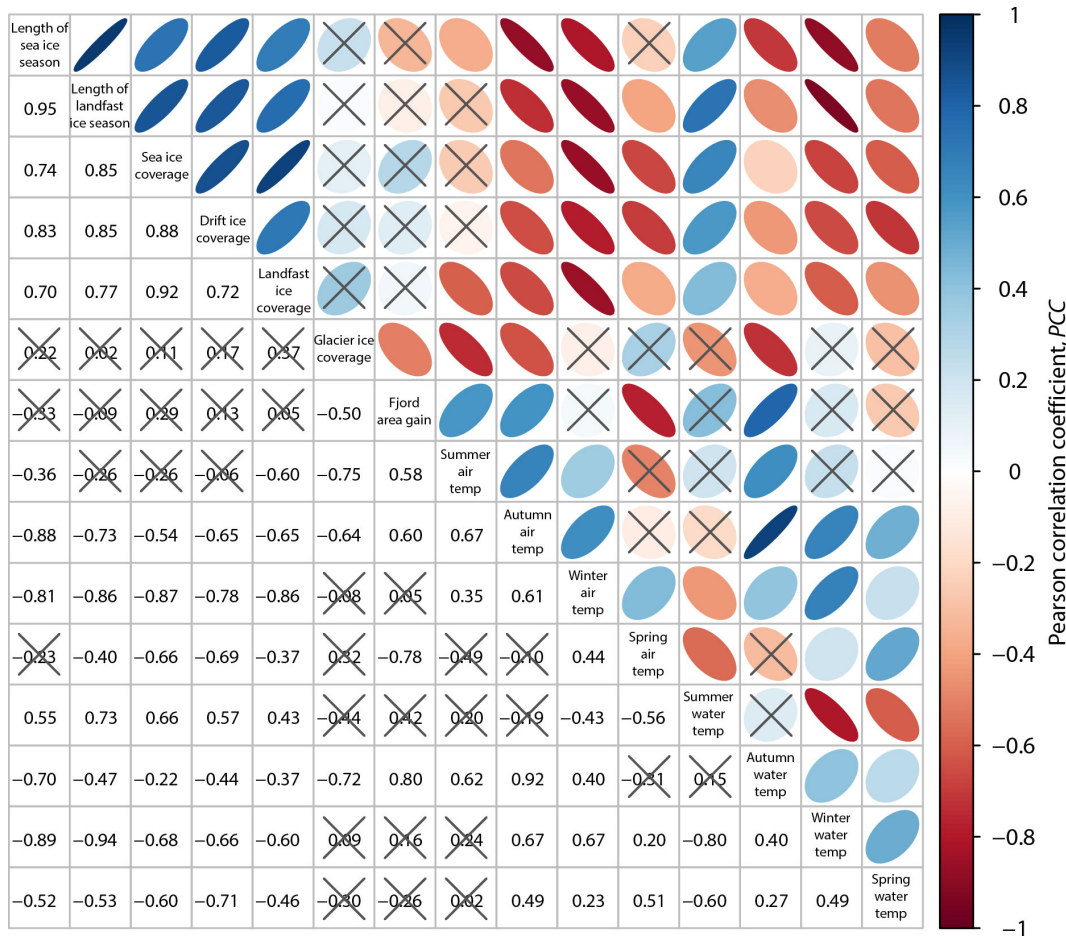
Figure 15. Matrix of correlation coefficients and best-fit ellipses for ice parameters and environmental forcings obtained for seasons with complete observations using the Pearson correlation in R. The Pearson correlation coefficient (PCC) is represented by the colour bar and describes both the strength (absolute value) and sign of relationships. Strength and sign of relationships are also represented by, respectively, width and orientation of the ellipses. Insignificant relationships ($p > 0.05$) are crossed out. Temperatures refer to the mean monthly for July–September (summer), October–December (autumn), January–March (winter) and April–June (spring). For the values and units see Tables 2, 5, 6 and 7.

26 % fjord surface), landfast ice (3.1 %–40 %) and glacier ice (3.7 %–5.2 %) from year to year, with no clear long-term trend as demonstrated using the Mann–Kendall test.

There was a statistically significant negative correlation between the water temperature in winter months and the length of the sea ice and landfast ice season, as well as between the air temperature in winter months and sea ice and landfast ice coverage. Glacier ice coverage depended on summer months air and autumn months water temperatures where lower temperatures enhanced ice persistence. Fjord area gain was faster when autumns were warmer and springs were cooler.

The unprecedented dataset of near-daily high-resolution ice type maps over 11.5 years can be used in in a range of studies including modelling of fjord water circulation, wave transformation and runup, coastal flooding and erosion, and fjord ecology, as well as PPS management and boat/snowmobile transportation planning.

References

Arntsen, M., Sundfjord, A., Skogseth, R., Błaszczyk, M., and Promińska, A.: Inflow of warm water to theinner Hornsund fjord, Svalbard: Exchange mechanisms and influenceon local sea ice cover and glacier frontmelting, Journal of Geophysical Research: Oceans, 124, 1915–1931, https://doi.org/10.1029/2018JC014315, 2019.

Błaszczyk, M., Jania, J. A., and Kolondra, L.: Fluctuations of tidewater glaciers in Hornsund fjord (southern Svalbard) since the beginning of the 20th century, Polar Research, 34, 327–352, https://journals.pan.pl/dlibra/publication/114504/edition/99557/content (last access: 27 January 2025), 2013.

Casas-Prat, M. and Wang, X. L.: Projections of extreme ocean waves in the Arctic and potential implications for coastal inundation and erosion, J. Geophys. Res. Oceans, 125, e2019JC015745, https://doi.org/10.1029/2019JC015745, 2020.

Cristea, A., van Houtte, J., and Doulgeris, A. P.: Integrating Incidence Angle Dependencies Into the Clustering-Based Segmentation of SAR Images, IEEE J. Sel. Top. Appl., 13, 2925–2939, https://doi.org/10.1109/JSTARS.2020.2993067, 2020.

de Steur, L., Sumata, H., Divine, D. V., Granskog, M. A., and Pavlova O.: Upper ocean warming and sea ice reduction in the East Greenland Current from 2003 to 2019, Commun. Earth Environ., 4, 261, https://doi.org/10.1038/s43247-023-00913-3, 2023.

Dierking, W., Lang, O., and Busche, T.: Sea ice local surface topography from single-pass satellite InSAR measurements: a feasibility study, The Cryosphere, 11, 1967–1985, https://doi.org/10.5194/tc-11-1967-2017, 2017.

Gao, T., Lan, C., Zhou, C., Zhang, Y., Huang, W., Wang, Y., and Wang, L.: Arctic sea ice motion retrieval from multisource SAR images using a keypoint-free feature tracking algorithm, ISPRS Journal of Photogrammetry and Remote Sensing 230, 258–274, https://doi.org/10.1016/j.isprsjprs.2025.09.013, 2025.

Grabiec, M., Ignatiuk, D., Jania, J. A., Moskalik, M., Głowacki, P., Błaszczyk, M., Budzik, T., and Walczowski, W.: Coast formation in an Arctic area due to glacier surge and retreat: The Hornbreen–Hambergbreen case from Spistbergen, Earth Surf. Process. Land., 43, 387–400, https://doi.org/10.1002/esp.4251, 2018.

Guo, W., Landy, J., Lohse, J., Doulgeris, A. P., Johansson, M., Eltoft, T., Itkin, P., and Xu, S.: Toward a Multidecadal SAR Analysis of Sea Ice Types in the Atlantic Sector of the Arctic Ocean, IEEE Journal of Selected Topics in Applied Earth Observations and Remote Sensing, 18, 10486–10502, https://doi.org/10.1109/JSTARS.2025.3555864, 2025.

Herman, A., Wojtysiak, K., and Moskalik, M.: Wind wave variability in Hornsund fjord, west Spitsbergen, Estuar. Coast. Shelf S., 217, 96–109, https://doi.org/10.1016/j.ecss.2018.11.001, 2019.

Herman, A., Swirad, Z. M., and Moskalik, M.: Increased exposure of the shores of Hornsund (Svalbard) to wave action due to a rapid shift in sea ice conditions, Elementa: Science of the Anthropocene, 13, 00067, https://doi.org/10.1525/elementa.2024.00067, 2025.

Johansson, A. M., Malnes, E., Gerland, S., Cristea, A., Doulgeris, A. P., Divine, D. V., Pavlova, O., and Lauknes, T. R.: Consistent ice and open water classification combining historical synthetic aperture radar satellite images from ERS-1/2, Envisat ASAR, RADARSAT-2 and Sentinel-1A/B, Ann. Glaciol., 61, 40–50, https://doi.org/10.1017/aog.2019.52, 2020.

Kendall, M. G.: Rank correlation methods, 4th edn., Charles Griffin, London, UK, ISBN 9780852641996, 1970.

Kim, M., Kim, H.-C., Im, J., Lee, S., and Han, H.: Object-based landfast sea ice detection over West Antarctica using time series ALOS PALSAR data, Remote Sens. Environ., 242, 111782, https://doi.org/10.1016/j.rse.2020.111782, 2020.

Korosov, A. A. and Rampal, P. A.: Combination of Feature Tracking and Pattern Matching with Optimal Parametrization for Sea Ice Drift Retrieval from SAR Data, Remote Sensing, 9, 258, https://doi.org/10.3390/rs9030258, 2017.

Larsen, Y., Engen, G., Lauknes, T., Malnes, E., and Høgda, K.: A generic differential interferometric SAR processing system, with

applications to land subsidence and snow-water equivalent retrieval, Fringe 2005 Workshop, 610, ISBN 92-9092-921-9, 2006.

Liu, S., Xu, S., Guo, W., Fan, Y., Zhou, L., Landy, J., Johansson, M., Zhu, W., and Petty, A.: On the statistical relationship between sea ice freeboard and C-band microwave backscatter – a case study with Sentinel-1 and Operation IceBridge, The Cryosphere, 19, 5175–5199, https://doi.org/10.5194/tc-19-5175-2025, 2025.

Lohse, J., Doulgeris, A., and Dierking, W.: An optimal decision-tree design strategy and its application to sea ice classification from SAR imagery, Remote Sensing, 11, 1574, https://doi.org/10.3390/rs11131574, 2019.

Loose, B., Fer, I., Ulfsbo, A., Chierici, M., Droste E. S., Nomura, D., Fransson, A., Hoppema, M., and Torres-Valdes, S.: An analysis of air-sea gas exchange for the entire MOSAiC Arctic drift, Elementa: Science of the Anthropocene, 12, 1, https://doi.org/10.1525/elementa.2023.00128, 2024.

Lubin, D. and Massom, R.: Polar Remote Sensing, Volume I: Atmosphere and Oceans, Springer-Verlag, Berlin Heidelberg New York, Praxis Publishing Ltd., Chichester, ISBN 9783662499762, 2006.

Luckman, A., Benn, D. I., Cottier, F., Bevan, S., Nilsen, F., and Inall, M.: Calving rates at tidewater glaciers vary strongly with ocean temperature, Nat. Commun., 6, 8566, https://doi.org/10.1038/ncomms9566, 2015.

Makhotina, E., Rees, G., Swirad, Z., and Tutubalina, O.: Mapping of sea and glacier ice distribution in 2018-2023 in the Hornsund fjord, Svalbard with PlanetScope imagery, EGU General Assembly 2025, Vienna, Austria, 27 Apr–2 May 2025, EGU25-7127, https://doi.org/10.5194/egusphere-egu25-7127, 2025.

Mann, H. B.: Nonparametric tests against trend, Econometrical, 13, 245–259, 1945.

Mezzina, B., Goosse, H., Klein, F., Barthélemy, A., and Massonnet, F.: The role of atmospheric conditions in the Antarctic sea ice extent summer minima, The Cryosphere, 18, 3825–3839, https://doi.org/10.5194/tc-18-3825-2024, 2024.

Muckenhuber, S. and Sandven, S.: Open-source sea ice drift algorithm for Sentinel-1 SAR imagery using a combination of feature tracking and pattern matching, The Cryosphere, 11, 1835–1850, https://doi.org/10.5194/tc-11-1835-2017, 2017.

Muckenhuber, S., Nilsen, F., Korosov, A., and Sandven, S.: Sea ice cover in Isfjorden and Hornsund, Svalbard (2000–2014) from remote sensing data, The Cryosphere, 10, 149–158, https://doi.org/10.5194/tc-10-149-2016, 2016.

Muilwijk, M., Hattermann, T., Martin, T., and Granskog, M. A.: Future sea ice weakening amplifies wind-driven trends in surface stress and Arctic Ocean spin-up, Nature Communications, 15, 6889, https://doi.org/10.1038/s41467-024-50874-0, 2024.

Nomura, D., Granskog, M. A., Fransson, A., Chierici, M., Silyakova, A., Ohshima, K. I., Cohen, L., Delille, B., Hudson, S. R., and Dieckmann, G. S.: CO_2 flux over young and snow-covered Arctic pack ice in winter and spring, Biogeosciences, 15, 3331–3343, https://doi.org/10.5194/bg-15-3331-2018, 2018.

NPI: Kartdata Svalbard 1 : 100 000 (S100 Kartdata)/Map Data, Norwegian Polar Institute [data set], https://doi.org/10.21334/npolar.2014.645336c7, 2014.

Park, J.-W., Korosov, A. A., Babiker, M., Won, J.-S., Hansen, M. W., and Kim, H.-C.: Classification of sea ice types in Sentinel-1 synthetic aperture radar images, The Cryosphere, 14, 2629–2645, https://doi.org/10.5194/tc-14-2629-2020, 2020.

Pętlicki, M., Ciepły, M., Jania, J. A., Promińska, A., and Kinnard, C.: Calving of tidewater glacier driven by melting at the waterline, J. Glaciol., 61, 851–863, https://doi.org/10.3189/2015JoG15J062, 2015.

Promińska, A., Falck, E., and Walczowski, W.: Interannual variability in hydrography and water mass distribution in Hornsund, an Arctic fjord in Svalbard, Polar Res., 37, 1495546, https://doi.org/10.1080/17518369.2018.1495546, 2018.

Ricker, R., Kauker, F., Schweiger, A., Hendricks, S., Zhang, J., and Paul, S.: Evidence for an Increasing role of ocean heat in Arctic winter sea ice growth, J. Climate, 34, 5215–5227, https://doi.org/10.1175/JCLI-D-20-0848.1, 2021.

Rodzik, J. and Zagórski, P.: Shore ice and its influence on development of shores of the southwestern Spitsbergen, Oceanol. Hydrobiol. S., 38, 163–180, 2009.

Roquet, F., Ferreira, D., Caneill, R., Schlesinger, D., and Madec, G.: Unique thermal expansion properties of water key to the formation of sea ice on Earth, Science Advances, 8, https://doi.org/10.1126/sciadv.abq0793, 2022.

Saloranta, T. M. and Svendsen, H.: Across the Arctic front west of Spitsbergen: high-resolution CTD sections from 1998–2000, Polar Res., 20, 177–184, https://doi.org/10.3402/polar.v20i2.6515, 2001.

Spreen, G., de Steur, L., Divine, D., Gerland, S., Hansen, E., and Kwok, R.: Arctic sea ice volume export through Fram Straight from 1992 to 2014, Journal of Geophysical Research: Oceans, 125, e2019JC016039, https://doi.org/10.1029/2019JC016039, 2020.

Styszyńska, A. and Rozwadowska, A.: Ice conditions in Hornsund and its foreshore (south-west Spitsbergen) during winter season 2006/07, Problemy Klimatologii Polarnej, 18, 141–160, 2008 (in Polish).

Swirad, Z. M.: Ice type maps for Hornsund, Svalbard, 1.2012-6.2023 (v1.0), Zenodo [data set], https://doi.org/10.5281/zenodo.15647080, 2025.

Swirad, Z. M., Johansson, A. M., and Malnes, E.: Ice distribution in Hornsund fjord, Svalbard from Sentinel-1A/B (2014–2023), PANGAEA [data set], https://doi.org/10.1594/PANGAEA.963167, 2023a.

Swirad, Z. M., Moskalik, M., and Herman, A.: Wind wave and water level dataset for Hornsund, Svalbard (2013–2021), Earth Syst. Sci. Data, 15, 2623–2633, https://doi.org/10.5194/essd-15-2623-2023, 2023b.

Swirad, Z. M., Johansson, A. M., and Malnes, E.: Extent, duration and timing of the sea ice cover in Hornsund, Svalbard, from 2014–2023, The Cryosphere, 18, 895–910, https://doi.org/10.5194/tc-18-895-2024, 2024a.

Swirad, Z. M., Johansson, A. M., and Malnes, E.: Ice distribution in Hornsund fjord, Svalbard from RADARSAT-2 (2012–2016), PANGAEA [data set], https://doi.org/10.1594/PANGAEA.969031, 2024b.

van Pelt, W., Pohjola, V., Pettersson, R., Marchenko, S., Kohler, J., Luks, B., Hagen, J. O., Schuler, T. V., Dunse, T., Noël, B., and Reijmer, C.: A long-term dataset of climatic mass balance, snow conditions, and runoff in Svalbard (1957–2018), The Cryosphere, 13, 2259–2280, https://doi.org/10.5194/tc-13-2259-2019, 2019.

Wang, Q., Lohse, J. P., Doulgeris, A. P., and Eltoft, T.: Data augmentation for SAR sea ice and water classifica-

tion based on per-class backscatter variation with incidence angle, IEEE Trans. Geosci. Remote Sens., 61, 4205915, https://doi.org/10.1109/TGRS.2023.3291927, 2023.

Wang, X., Zhang, Z., Wang, X., Vihma, T., Zhou, M., Yu, L., Uotila, P., and Sein, D. V.: Impacts of strong wind events on sea ice and water mass properties in Antarctic coastal polynyas, Climate Dynamics, 57, 3505–3528, https://doi.org/10.1007/s00382-021-05878-7, 2021.

Wawrzyniak, T. and Osuch, M.: A 40-year High Arctic climatological dataset of the Polish Polar Station Hornsund (SW Spitsbergen, Svalbard), Earth Syst. Sci. Data, 12, 805–815, https://doi.org/10.5194/essd-12-805-2020, 2020.

Wojtysiak, K., Herman, A., and Moskalik, M.: Wind wave climate of west Spitsbergen: Seasonal variability and extreme events, Oceanologia, 60, 331–343, https://doi.org/10.1016/j.oceano.2018.01.002, 2018.

Zagórski, P., Rodzik, J., Moskalik, M., Strzelecki, M. C., Lim, M., Błaszczyk, M., Promińska, A., Kruszewski, G., Styszyńska, A., and Malczewski, A.: Multidecadal (1960–2011) shoreline changes in Isbjørnhamna (Hornsund, Svalbard), Pol. Polar Res., 36, 369–390, https://journals.pan.pl/Content/99617/PDF/10183_Volume36_Issue4_05_paper.pdf (last access: 8 July 2025), 2015.

Zhu, T., Cui, X., and Zhang, Y.: A High-Resolution Sea Ice Concentration Retrieval from Ice-WaterNet Using Sentinel-1 SAR Imagery in Fram Strait, Arctic, Remote Sensing, 17, 3475, https://doi.org/10.3390/rs17203475, 2025.